Phenotypic plasticity in coral skeletal features: Molecular signatures from DNA methylation and transcriptional interaction networks

Running Title: Induced phenotypic plasticity and methylome repatterning.

Kelly Gomez-Campo[1*], Robersy Sanchez[1], Isabel Martínez-Rugerio[1], Xiaodong Yang[1], Tom Maher[1], C. Cornelia Osborne[1], Susana Enriquez[3], Iliana B. Baums[1,4], Sally A. Mackenzie[1,2], Roberto Iglesias-Prieto[1*]

[1]Department of Biology, The Pennsylvania State University, University Park, PA 16802, USA

[2]Department of Plant Science, The Pennsylvania State University, University Park, PA 16802, USA

[3]Unidad Académica de Sistemas Arrecifales Puerto Morelos, Instituto de Ciencias del Mar y Limnología, Universidad Nacional Autónoma de México, 77580, México

[4] Helmholtz Institute for Functional Marine Biodiversity, Ammerlaender Heerstrasse 231, 26129 Oldenburg, Germany

*Correspondence to: kjg27@psu.edu (K.G.C.); rzi3@psu.edu (R.I.P).

Author contributions: R.I.P., I.B.B., S.A.M. and K.G.C. conceived and designed the experiments. K.G.C performed the experiments, integrated, and analyzed the data. I.B.B., S.A.M., R.S., and X.Y. contributed to genomic-epigenomic analysis and interpretations. S.A.M. and R.S. to Methyl-IT and biological network analyses. R.I.P. and S.E. to phenotypic descriptions interpretation. I.M.R. assisted in field work and phenotypic descriptions. T.M. assisted in methylation computational work. C.C.O. assisted in laboratory and gene expression computational work. K.G.C and R.I.P. wrote the manuscript. K.G.C, S.E., I.B.B, S.A.M., R.I.P. reviewed and edited the manuscript. Funding acquisition: R.I.P., I.B.B., S.A.M. All authors approved the manuscript.

Competing Interest Statement: Authors declare no competing interests.

Classification: Biological Sciences, Ecology, Genetics, Physiology

Keywords: Phenotypic plasticity, DNA methylation, gene expression, biological networks, biomineralization.

This PDF file includes:

      Main Text
      Figures 1 to 6

30

Abstract

31

32 Acclimation through phenotypic plasticity represents a more rapid response to environmental change than

33 adaptation and is vital to optimize organisms' performance in different conditions. Generally, animals are

34 less phenotypically plastic than plants, but reef-building corals exhibit plant properties. They are light-

35 dependent with a sessile and modular construction that facilitates rapid morphological changes within their

36 lifetime. We induced phenotypic changes by altering light exposure in a reciprocal transplant experiment

37 and found that coral plasticity is a colony trait emerging from comprehensive morphological and

38 physiological changes at the local level. Plasticity in skeletal features optimized coral light harvesting and

39 utilization and paralleled with significant methylome and transcriptome modifications. Network-associated

40 responses resulted in the identification of hub genes and clusters associated to the change in phenotype:

41 inter-partner recognition and phagocytosis, soft tissue growth and biomineralization. Furthermore, we

42 identified hub genes putatively involved in animal photoreception-phototransduction. These findings

43 fundamentally alter our understanding of how cnidarian invertebrates repattern the methylome and adjust

44 a phenotype, revealing an important role of light sensing by the coral animal to optimize photosynthetic

45 performance of the symbionts.

46 **Significance Statement**

47 Stony corals shape the benthic topography of the ocean by the net accumulation of calcium carbonate,

48 engineering biodiversity hotspots that provide food security, livelihood opportunities, and protection from

49 coastal erosion worldwide. Corals optimize growth through morphological plasticity, however, genomic

50 and epigenomic underpinnings of such plasticity are largely unknown. We applied comprehensive

51 biometrics, machine learning to identify divergent methylation, and methylome-transcriptome-derived

52 network analyses. We revealed an extraordinary number of hub genes likely to be integral to morphologic

53 plasticity. Accordingly, DNA methylation may represent an important mechanism facilitating the evolution

54 of the biomineralization process. The integration of methylation and transcriptional information makes

2

55   significant inroads in the identification of networks underpinning phenotypic changes and provides a

56   roadmap for studies of non-model organisms.

57　**Main Text**

58　**Introduction**

59　　　　The modification of an organism's physical features (phenotype) through development and growth

60　is affected by the interaction of gene expression (genotype) with environmental cues. This capacity for

61　phenotypic plasticity allows organisms to optimize their physiological performance under different

62　environmental conditions (Chevin et al., 2010; Nicotra et al., 2010; Torda et al., 2017). While most organisms

63　exhibit some degree of plasticity, the sessile condition of plants prevents movement to new environments if

64　conditions become unfavorable. Consequently, they have evolved broad plasticity in their physical

65　characteristics, such as leaf size or shape, root architecture or reproductive behaviors, to cope with

66　changing environments and maintain optimal light harvesting (Borges, 2008). Animals generally exhibit far

67　less plasticity than plants; except for reef-building corals. With similar life-histories to plants, their colonies

68　display high levels of morphological plasticity.

69　　　　Corals are modular, sessile organisms responsible for the net accumulation of calcium carbonate

70　in coral reefs. The power to calcify is the result of animals acquiring photosynthetically-fixed carbon through

71　an obligate symbiosis with dinoflagellates (or microalgae) (family Symbiodiniaceae) (Falkowski et al., 1984;

72　Gattuso et al., 1999; LaJeunesse et al., 2018; Trench, 1993). This means that corals, much like plants,

73　make their living from light capture. The metabolic integration is such that coral skeletons evolved to be

74　efficient light collectors (Enríquez et al., 2017) with skeletal morphology adjusted in response to depth-

75　dependent light availability (Malik et al., 2021). It is, therefore, not surprising that corals exhibit molecular

76　signatures for perceiving and responding rapidly to changes in light availability.

77　　　　While observed phenotypic plasticity is shaped by the interaction between genomes and

78　environments, the role of epigenomes in this plasticity has captivated the interest of biologists. Phenotypic

79　adjustments induced by environmental cues and gene expression may be influenced by chromatin factors

80　like DNA cytosine methylation, a dynamic feature of many eukaryotic genomes, including plants, animals,

81　and fungi. DNA methylation is a process where methyl groups are added to cytosine bases of the DNA

82　molecule and, in association with histone modifications, modify chromatin conformation (Buitrago et al.,

83   2021; Hashimshony et al., 2003). High-density methylation within promoter regions can silence genes,

84   whereas lower-density intragenic methylation repatterning can influence alternative splicing activity, leading

85   to changes in an organism's phenotype (Bossdorf et al., 2010; Lev Maor et al., 2015). This is a reversible

86   process influenced by environmental conditions, hence allowing phenotypic plasticity to occur (Verhoeven

87   et al., 2010, 2016). Moreover, methylation repatterning accompanies chromatin response to environmental

88   changes without altering the DNA sequence and with the potential for heritable transmission. The

89   repatterning is generally associated with other epigenetic effects such as histone modifications and changes

90   in noncoding RNA. These methylome modifications can be assayed at single nucleotide resolution,

91   providing the robust datasets required for identifying responsive underlying gene networks that could explain

92   phenotypic adjustments (Hafner & Mackenzie, 2023; Kundariya et al., 2022; Sanchez et al., 2019; Sanchez

93   & Mackenzie, 2016a, 2020; Yang & Mackenzie, 2020).

94   DNA methylation is evolutionarily ancient; however, its distribution and functions are diverse,

95   debatable, or unknown among taxa. In plants, phenotypic plasticity and its heritability has been associated

96   with changes in DNA methylation patterns (Verhoeven et al., 2010, 2016), but the functional significance in

97   coral phenotypic plasticity is still tenuous. Several studies have associated coral DNA methylation with

98   plasticity (Dimond et al., 2017; Dimond & Roberts, 2016; Dixon et al., 2018; Durante et al., 2019; Liew et

99   al., 2018a; Putnam et al., 2016; Roberts & Gavery, 2012; Rodríguez-Casariego et al., 2020), with whole-

100 genome bisulfite sequencing (WGBS) contributing to single base-pair resolution (Liew et al., 2018a).

101 However, WGBS data analysis can be challenging due to the highly dynamic features of methylome

102 datasets. This stochasticity has complicated discrimination of treatment-associated signal from natural

103 background variation, and the understanding of treatment-associated phenotypic adjustments with

104 methylome modifications (Hafner & Mackenzie, 2023; Yang & Mackenzie, 2020). As advances in

105 computational biology demonstrate the effect of single cytosine changes in phenotypic responses, novel

106 methods have been addressing challenges in conventional methodologies (Hafner & Mackenzie, 2023;

107 Kundariya et al., 2022; Sanchez et al., 2019; Sanchez & Mackenzie, 2016a, 2020; Yang & Mackenzie,

108 2020). One approach to discriminate treatment-associated differential methylation is to incorporate signal

109 detection and machine learning (Hafner & Mackenzie, 2023; Kundariya et al., 2022; Sanchez et al., 2019;

Sanchez & Mackenzie, 2016a, 2016b) with MethyIT (R package Methyl-IT 0.3.1.2, (Sanchez et al., 2019)). The approach treats methylation data as probability distributions, permitting variation within multiple control samples to be subtracted from the treatment datasets to discriminate treatment-specific variation. Machine learning then permits validation of treatment association with over 98% confidence. Further validation of this approach is accomplished, in models like Arabidopsis, with incorporation of mutations in the RNA-directed DNA methylation pathway (Kundariya et al., 2022). However, the approach is especially valuable in non-model systems where changes cannot be confirmed with targeted mutation(s). The association between phenotype change and treatment-associated methylome modification is informative in understanding the underlying molecular features of the phenotypic change by directly identifying responsive gene networks (Hafner & Mackenzie, 2023; Kundariya et al., 2022; Sanchez et al., 2019; Sanchez & Mackenzie, 2016a, 2016b).

To examine the phenotype to methylome association, we conducted a reciprocal transplant experiment to induce light-mediated phenotypic responses in the reef-building Elkhorn coral *Acropora palmata* and investigated DNA methylation and transcriptional responses potentially responsible for plasticity. Extensive biometrics revealed not only changes in coral tissue pigmentation and metabolic rates but also in skeletal morphology after five weeks. This skeletal remodeling was accompanied by intragenic methylome repatterning, discovered by signal detection with machine learning-based analysis. We further integrated differentially methylated (DMG) and expressed (DEG) gene datasets to elucidate how light responses integrate into gene regulatory networks controlling functional traits. By exploring the resulting hub genes and gene clusters, we were able to predict functional associations with observed phenotype changes and identify markers of plasticity in reef-building corals. Moreover, our results contribute to emerging evidence that epigenetics contribute to the machinery that can alter DNA structure during skeletal remodeling in metazoans.

Results and Discussion

Corals exploit intra-colonial environmental differences through plasticity

The branching coral *Acropora palmata* is the dominant reef-builder on shallow, wave-exposed Caribbean reefs. Colonies exhibit tree-like morphologies with strong intra-colonial light gradients ranging from 3 to 100% of sub-superficial irradiance (E_s). In our experiment, we quantified intra-colonial phenotypic plasticity by measuring traits from High Light (HL) surfaces (fragments from upperside surfaces of branches, n = 12) exposed to 70% of E_s and Low Light (LL) surfaces (fragments from underside surfaces of branches, n =12) exposed to 3-7% of E_s (**Fig. 1A, Table 1**). Structural, optical, and physiological traits of HL and LL fragments releveled two distinct phenotypes. HL phenotypes had significantly greater total polyp density (**Fig. 1F**), density of taller corallites (**Fig. 1G**), total host protein (**Fig. 1H**) and algal density (**Fig 1I**). Surfaces with taller corallites can favor the formation of internal light gradients, increase levels of pigment self-shading, and reduce the proportion of polyp-surface exposed to the external high-light levels (Enríquez et al., 2017; Ow & Todd, 2010). In contrast, LL phenotypes showed a small number of short corallites that can facilitate the lateral spread of light.

We expected these differences in skeletal features to affect how corals collect and utilize light for colony growth. To disentangle this, we used algal symbiont density, chlorophyll *a* (chl*a*), host soluble proteins, and *in vivo* light absorption of the intact coral tissue (**Table S1**) to describe light absorption efficiency of HL and LL phenotypes. We estimated three optical traits: a^*_{Chla} (m^2 mg Chla^{-1}), which describes the holobiont's efficiency to absorb light (Enríquez et al., 2005a), a^*_{sym} (m^2 sym^{-1}) that describes *in hospite* light absorption efficiency of the algal symbionts, and a^*_M (cm^2 mg protein^{-1}) indicative of the potential return for the host (mass) of the energy absorbed (Falkowski et al., 1985; Scheufen et al., 2017) (**Table S1**). We detected less algal cell densities (**Fig. 1I**) but more chl*a* per cell in LL phenotypes (**Fig. 1J**), and opposite traits in HL phenotypes. This resulted in equal chl*a* concentration in both HL and LL phenotypes (**Fig 1K**). These findings contradict the assumption that more light always induces lower pigmentation in multicellular photosynthetic organisms and confirms the ability of coral skeletal features to rewire the algal light environment. Conversely, a^*_{Chla} showed that both phenotypes of the coral colony are equally efficient in absorbing light (**Table S1**), a response reached by adjusting skeletal features.

160   *A. palmata* exploits a wide range of light environments without changing its symbiont species

161   (*Symbiodinium 'fitti'*), (Baums et al., 2014) in contrast to other reef-building corals (Kemp et al., 2015).

162   Instead, *A. palmata* colonies fine-tune structural traits; algal density, chl*a* density, and skeletal morphology

163   (**Fig. 1).** This mechanism minimizes "pigment packing" in underside surfaces in response to LL conditions,

164   resulting in light collectors as efficient as those of HL surfaces. Although photosynthesis is more active on

165   upper side surfaces (**Fig. 1N**), the ratio of photosynthesis/respiration (P/R = 3), photosynthetic efficiency

166   (**Fig. 1L**) and minimum quantum requirement (**Table S1**) were similar in both sides of branches. These

167   observations further highlight the ability of *A. palmata* to optimize light absorption and utilization through

168   plasticity as a central strategy to exploit the strong intra-colonial light gradient and maximize colony

169   productivity for growth.

Induced morphological plasticity with reciprocal transplants

171   *A. palmata* frequently reproduce asexually via branch fragmentation, a result of physical disturbance

172   (*i.e.* waves and storms) (Baums et al., 2006). Branches are often turned upside down when they land on the

173   benthos. Fragmentation thus induces strong and rapid changes in light regimes, where survival is dependent

174   on their successful acclimatization to the new light conditions. Presumably, upper and underside branch

175   surfaces interchange phenotypes through acclimation to new light regimes. We took advantage of this life

176   history trait to induce plasticity by altering light exposure in a reciprocal transplant experiment (see Methods,

177   **Fig. 2A**). Coral fragments from three colonies representing three distinct genets (detected with Standard

178   Tools for Acroporid Genotyping STAGdb (Kitchen et al., 2020)) were manipulated, so that HL phenotypes

179   (n = 21) and LL phenotypes (n = 21) experienced unchanged light fields, and treated fragments were

180   switched to the opposite light condition HL→LL (High Light to Low Light, n = 21) and LL→HL (Low Light to

181   High Light, n = 21) (**Fig. 2A**). Within 5 weeks, treated coral fragments significantly adjusted their phenotype.

182   The acclimation was gradual (tracked by visual inspection), and transplants became increasingly similar in

183   morphology to coral surfaces of the destination light condition (**Fig. 2C, Fig. S4**), comparable to what is

184   observed when coral colonies are transplanted along depth gradients (Malik et al., 2021). Pressure over

185   photosystem II (Q_m), metabolic rates and visual growth indicated that corals acclimated successfully to the

186   destination light conditions (**Fig. 2B, C, Table S1**). Interestingly, a*$_{Chla}$, the holobiont's efficiency to absorb

187   light, indicated that fragments may continue changing pigmentation and skeletal features to fully optimize

188   performance (**Fig. 2D, E**). Nonetheless, most significant changes were observed in skeletal features (taller

189   corallites per area), polyp density and the balance between chl*a* density and symbiont density (**Fig. 2, Table**

190   **S1**). Significant differences were found among the 4 group conditions ($R = 0.336$, $P<0.001$, **Fig. S5**),

191   suggesting a response driven by light-mediated phenotypes and not the genet ($R = 0.188$, $P> 0.05$).

192   Phenotypic plasticity was induced by altering ~80% of light availability (~18 mol quanta m^{-2} day^{-1}).

193   These were drastic changes that are nevertheless commonly experienced by coral species during their life

194   cycle. Whole colony metabolic performance is optimized by adjustments at the module (polyp) level for

195   resource acquisition. Similarly, phenotypic plasticity in plants results from a local response (*e.g.* of shaded

196   branches) which optimizes light harvesting and utilization for growth (De Kroon et al., 2005). While corals

197   are colonial animals, and each polyp (module) is akin to an individual organism, a coral's response to the

198   light environment should consider the integrated response to local conditions experienced by local modules.

199   Accordingly, modular plasticity may be one evolving trait under selection, as has been suggested for plants

200   (De Kroon et al., 2005).

201   **Reading the methylome with Methyl-IT: Light-mediated methylome repatterning**

202   Following induced light-mediated phenotypic plasticity, we investigated DNA methylome response to

203   coral group conditions (n = 8 per group condition). With WGBS (30X coverage), we documented methylation

204   of the *A. palmata* genome. We identified CpG context methylation (~14%) to be higher in the *A. palmata*

205   than in any other invertebrate (Liew et al., 2018a; Pelizzola & Ecker, 2011). We detected insignificant levels

206   of methylation in CHG or CHH context (<0.6%) (H = A, T, or C) (**Fig. 3A**), and CpG methylation was

207   prevalent in genic regions (**Fig. 3B**) as previously reported in other coral species (Dimond & Roberts, 2016;

208   Dixon et al., 2018; Liew et al., 2018a).

209   To associate the observed coral phenotypic plasticity with high-resolution DNA methylome variation,

210   we used a signal detection-machine learning approach (R package Methyl-IT 0.3.1.2) (Sanchez et al.,

211 2019), designed to discriminate methylation signal induced by environmental variation at individual cytosine

212 positions (Sanchez et al., 2019; Sanchez & Mackenzie, 2020; Yang et al., 2020). We assessed gene-

213 associated, differentially methylated positions (DMPs) with no regard to methylation density, context, or

214 directionality (hypo/hypermethylation) (Methods, **Fig. 3C**). Parallel analysis of DMP variation within control

215 samples allowed discrimination of treatment-associated DMPs and their classification on the basis of

216 hierarchical clustering (HC) and principal component analysis (PCA) (Methyl-IT), which enabled an

217 unbiased view of methylome repatterning (**Fig. 3D**). There was significant separation of control and

218 treatment samples, indicating that light-mediated methylome modifications were driving the first two

219 principal components. Genes with the strongest discriminatory power from PC-scores in PC1 were

220 associated with cell cycle, extracellular matrix (ECM), regulation of transcription and transduction, and

221 biomineralization (**Table S2**).

222 **Agnostic biological network analysis with WGCNA: Network-based integration of DMG and DEG**
223 **datasets**

224 Significant coral phenotypic changes and gene-associated methylome repatterning warranted deeper

225 investigation to uncover functional relationships with gene expression. We first identified DMGs (Methyl-IT

226 0.3.1.2) based on statistically significant differences in DMP counts from treated corals relative to control

227 groups (**Fig. S2**). RNA-sequencing was carried out on the same samples used for WGBS, with DEGs

228 identified (DESeq2 3.12.0.) via pairwise comparison between control and treatment groups. A total of 32

229 methylomes and 32 transcriptomes were analyzed with a range of 861 – 2255 DMGs and 1334 – 6479

230 DEGs detected (**Fig. S6**). We used a network-based approach to integrate the information, which provided

231 us with a collection of nodes and edges representing putative gene interactions (Albert, 2005). Since

232 network-based analyses can be influenced by the available annotation for a given species, we performed a

233 weighted correlation network analysis of coral gene expression and methylome modification (**Fig. S2**). To

234 understand the interaction between the change in methylomes (n = 32) and transcriptomes (n = 32), we

235 combined DMG and DEG datasets to one large dataset genes/coordinates. Dimensionality was reduced

236 with HC (**Fig. 4A**), PCA and a linear discriminant analysis. We assigned gene discriminatory power from

237   PC-scores (gene-score) (**Fig. S7**). The network was built in R-package Weighted Gene Correlation Network

238   Analysis (WGCNA 1.71) (Langfelder & Horvath, 2008), with visualization and statistical analysis in

239   Cytoscape 3.8.2 (Sanchez & Mackenzie, 2020). Network's centrality measures, edge weight, and node PC-

240   scores were included in clustering analyses to identify putative central regulators or hub genes. Hub loci are

241   critical network components, with loss or mutation predicted to cause breakdown of the network or lethality

242   to the organism (Albert, 2005; Sanchez & Mackenzie, 2020).

243   Methylome-transcriptome-derived gene network information revealed an extraordinary number of hub

244   genes likely to be integral to morphologic plasticity in symbiotic corals. General biological processes

245   included visual and sensory perception, growth and immunity, including carriers, transporters and receptors.

246   Two main cluster categories were identified (**Fig. 4B**). A Type I subnetwork (**Fig. 4C**) showed genes with

247   strong gene-gene interaction (edges with strongest correlation weights), denotating genes with similar

248   contribution to the change in phenotype. The main sub-network under this category was enriched in

249   Extracellular matrix (ECM) gene products, collagen-like domains, signaling activity, cell-cell adhesion and

250   EGF-domains, putatively associated with soft tissue growth and biomineralization (R-HSA-2022090, R-

251   HSA-1474244, R-HSA-1474290, R-HSA-2022090, R-HSA-388844, R-HSA-8849932). 139/199 genes in

252   this subnetwork were found to be differentially methylated, highlighting the influence of methylation to

253   changes in coral skeletal growth. Interestingly, we observed low gene-score values in this cluster, meaning

254   that individually each gene carries small proportion of the whole phenotypic variance. Seemingly, these

255   genes were co-methylated to give rise to a quantitative cumulative effect on phenotypic variation among

256   treatments, leading to the change in growth pattern, but with low discriminatory power individually.

257   Subnetworks Type II represented critical genes with the strongest discriminatory power, denoting hub

258   genes with strongest contribution to the change in phenotype (**Fig. 4D, E**). Accordingly, we considered these

259   loci to be strong candidates for biomarker identification. Annotated hub genes included $_{DEG}$*SLC7A2,*

260    $_{DEG}$*SLC22A13,* $_{DEG}$*SLC17A6B,* $_{DEG}$*PANP,* $_{DEG}$*IFI30,* $_{DEG}$*TRIM71,* $_{DEG}$*MELC2,* $_{DEG}$*ADAMTS18,* $_{DEG}$*CTRC,*

261    $_{DMG}$*HECTD4,* $_{DMG}$*LIPK,* $_{DEG}$*TNR,* $_{DMG}$*C0H691,* $_{DMG}$*TRPV6,* $_{DEG}$*HSP-16.2,* $_{DEG}$*SUSD2,* $_{DEG}$*COL6A5,*

262    $_{DEG}$*BTBD2,* $_{DEG}$*CASR* $_{DMG}$*GPR133,* $_{DMG}$*RABL6,* $_{DEG}$*PRSS27,* $_{DEG}$*SSTR5,* $_{DMG}$*MPDZ,* $_{DMG}$*SPTAN1,*

11

263 DEG*ABHD4,* DEG*COL12A1,* DEG*SPDEF,* DEG*HES4-a,* DEG*PTK7,* DEG*ASIC3* DEG*MFSD6,* DEG*COL11A1,*

264 DMG*CHMP6*, DEG*PRDM6*, DMG*FGFR1,* DMG*TMPRSS15,* DMG*TMPRSS11D,* DEG*B3GAT3*.

Predicted biological networks: network-associated responses from DMGs

266   We further aimed to investigate gene interactions in available experimental data by consulting

267 pathways from curated databases (Doncheva et al., 2019; Szklarczyk et al., 2017) to identify predicted

268 networks (see Methods; **Fig. S2**)*.* With the set of DMGs as input in *stringApp* (Cytoscape 3.8.2), we built a

269 baseline network and performed clustering analyses (with network centrality measures). Independent of the

270 destination light condition and genet, enriched function categories were posttranscriptional protein variants

271 (kw-0621 polymorphism, kw-0025 alternative splicing, kw-0597 phosphoprotein), cytoskeleton proteins (kw-

272 0206), calcium-dependent proteins (kw-0106 calcium), growth associated proteins (kw-0131 cell cycle, kw-

273 0965 cell-junction), and phagocytosis (kw-0966 cell projection) (**Fig. S8**). A common feature of main

274 candidate hub genes (**Fig. S8**, *ATR, PIF1, FANCD, SIRT1*) was DNA damage-repair-response (DRR), a

275 mechanism regulated by chromatin conformation. Chromatin remodeling complexes, at the core of DRR

276 (Stadler & Richly, 2017), are essential in DNA methylation patterning (Huck-Hui & Bird, 1999).

277   We used the set of DEGs to run the same network analyses separately (**Fig. S9**). However, we found

278 significant lower values of node Eigenvector of centrality (**Fig. S10**). This limited the identification of hubs

279 from gene expression data alone.

Predicted biological networks: network-associated responses from DMGs and DEGs.

281   The identification of key regulators in DMG sub-networks led us to investigate integrated DMG and

282 DEG networks in available experimental data and pathways from curated databases (Doncheva et al., 2019;

283 Szklarczyk et al., 2017). We detected sub-networks of hub genes contributing to phenotypic changes and

284 associated cellular processes, including inter-partner recognition and phagocytosis, regulation of host-

285 symbiont biomass, and calcification (reviewed in (Davy et al., 2012)). Sub-networks aligned with these

286 processes, independent of the destination light conditions and genet, and generally targeting the same

287 enriched categories, pathways, or protein families (**Fig. 5, Fig. S11-S14**). Network topology and node

hierarchy based on Eigenvector od Centrality suggested a general DMG-DEG interplay targeting key regulators (hubs) and triggering a cascade of responses, evident when source-sink nodes (**Fig. 5A** *CEP290*; **Fig. 5B** *THBS1*, *PTK2*, *SOX9*; **Fig. 5C** *RAB1A*; **Fig 5D** *ANAPC1*) interacted with strongly connected clusters.

Cells have mechanisms to detect specific environmental signals to transduce and trigger the appropriate responses. We identified a symbiont-independent photoreception-phototransduction sub-network (**Fig. 5A**, 51 nodes and 139 edges) potentially involved in animal sensing of a light stimulus (p-Cluster I). Network Enrichment Analysis (NEA) yielded mainly cilium assembly (GO.0060272, 19 enriched genes, FDR < 0.001). The putative hub gene $_{DMG-DEG}SPTAN1$ interacted with $_{DMG}CEP290$ and a transcriptional non-hub cluster (*USH2A, CRB1, EYS, MYO3A*) involved in phototransduction-reception. Interestingly, this sub-network further interacted with growth and calcification sub-networks (**Fig. 5B**). Previous work has elucidated the role of light in the coral animal independent symbiont metabolism. It was found that enhanced coral calcification but not photosynthesis occurs under blue light exposure (Cohen et al., 2016), and evidence suggests a light-mediated electrical potential in coral epithelia (Taubner et al., 2019). Moreover, Cnidaria constitutes the earliest branching phylum containing a well-developed visual system. Some jellyfish, like Cubozoa, have camera-type eyes with photoreceptor cells that are more similar to vertebrate than to invertebrate eyes (Kozmik et al., 2008). These findings suggest that coral animal photoreception-transduction is implicated in changes in growth pattern and skeletal features, although the role of photoreception-associated proteins is yet to be explored.

Consistent with significant changes in coral skeletal features for the optimization of light harvesting and utilization, we identified a coral growth and biomineralization sub-network (**Fig. 5B**, 86 nodes and 200 edges) that revealed NEA categories related to ECM proteins (KW-0272, 18 enriched genes, FDR < 0.001), cell-cell adhesion (KW-0130, 14 enriched genes, FDR < 0.001) and EGF-domains (KW-0245, 13 enriched genes, FDR < 0.001) as most prominent. From the sub-network of hub genes, integrin and spectrins interacted with glycoproteins and lipoproteins ($_{DMG}PTK2$, $_{DMG-DEG}THBS1$, and $_{DMG}LRP5$) involved in coral biomineralization (Drake et al., 2013; Gutner-Hoch et al., 2017; Hemond et al., 2014). Thrombospondin has

314 previously been suggested for its role in biomineral remodeling (Mummadisetti et al., 2021). Consistent with

315 this network topology, an important transcriptional interaction identified was SOX9, a transcription factor

316 (TF) with a role in skeletal development. Associated nodes involved TFs DEG*HIF1A*, DEG*HOPX*, and

317 DEG*FOXL1*, with the receptor protein DEG*NOTCH2* up regulated in this transcriptional interaction

318 (independent of the destination light condition). All hub genes interacted with a strongly connected cluster

319 of collagen-like domains that was mainly transcriptional and up-regulated when transplanted to HL, while

320 down-regulated when transplanted to LL. Collagen plays a structural role in the skeletal organic matrix

321 (SOM), and presence of SOM in calcifying organisms appears to be a prerequisite for the formation and

322 growth of biominerals (Allemand et al., 1998; Mummadisetti et al., 2021).

323   Holobiont biometrics showed the strong regulation of algal symbiont density by light-mediated

324 adjustments in skeletal features. These changes are achieved by phagocytosis-exocytosis-endocytosis with

325 associated innate immune recognition (Davy et al., 2012). We identified associated sub-networks with

326 enriched categories related to vesicle/vacuole-mediated transport (GO.0016192, 41 enriched genes, FDR

327 < 0.001) (**Fig. 5C**, 78 nodes and 174 edges). The core sub-network of hub genes (**Fig. 5C)** interacted with

328 spectrins, ankyrins, and key regulators of intracellular membrane traffic GTPases-RAB. Previous studies

329 have emphasized pattern recognition receptors (PRR) as key players in symbiosis establishment (Davy et

330 al., 2012). Main PPR identified are endocytosis mediator C-type lectin domain family member (DMG-

331 DEG*MRC1*) and Toll-like and Toll/interleukin-like receptors (DEG*TLR6* and DEG*TLR1*). Furthermore, we

332 identified a sub-network associated to immune system responses (NEA, HSA-1280218, 18 enriched genes,

333 FDR < 0.001) (**Fig. 5D**, 30 nodes and 195 edges), were hub genes (DMG-DEG*POLA1*, DMG*ATR*, DMG*PIF1*,

334 DMG*FBXO18*) interacted with the strongly connected component through an E3 ubiquitin ligase that targets

335 cell cycle regulatory proteins for degradation (DMG*ANAPC1*). The targeted cluster was mainly transcriptional

336 (both up- and down-regulated) and the few DMGs were also E3 ubiquitin ligases (DMG-DEG*HECTD1*,

337 DMG*HERC1*, DMG*HUWE1*).

338 **Concluding remarks**

339   Whole colony plasticity in the branching coral *A. palmata* resulted from the integration of modular

340   responses to local variation in light availability. The plasticity of local modules was evident when fragments

341   were transplanted to contrasting light environments, where significant changes in skeletal features prompted

342   the optimization of light absorption and utilization to maximize metabolic outputs and growth. Recognizing

343   this modular concept of plasticity is important in the face of heritability of colony-level traits versus local

344   module-level traits. Animal colonies consisting of many modules may remain coherent entities where colony

345   traits have the evolutionary potential to respond to natural selection (Simpson et al., 2020). Remarkably,

346   variants may arise locally, and single modules may have some evolutionary potential (Vasquez Kuntz et al.,

347   2022).

348   Local modular plasticity was accompanied by significant methylome and transcriptome modifications.

349   Enhanced resolution with the MethyIT pipeline allowed us to examine meaningful associations between a

350   natural phenotype, transcriptome and methylome modifications. Our data showed a significant light-

351   mediated change in coral morphology, a phenotypic adjustment that was reflected in molecular signatures

352   of changes in growth, including soft tissue growth and biomineralization. These observations suggest that

353   symbiotic corals have acquired the capability of effecting an epigenomic response that incorporates whole

354   methylome repatterning and is associated to changes in coral morphology. This interpretation aligns with

355   previous whole genome views that focused on the function of DNA methylation in phenotypic plasticity (Liew

356   et al., 2018b). The resolution allowed us to integrate genome-wide DNA methylation with gene expression

357   datasets into meaningful biological networks. Our comprehensive network approach based on interactions

358   from correlation matrix networks and gene interaction from curated databases for predicted networks offered

359   a powerful approach to identify potential markers of plasticity in the interaction of DMGs and DEGs.

360   Annotated genes *COL6A5, SPTAN1, PTK7, FGFR1, FBXO30, P4HA2, TNR, NID1, ITGAX, ANK3, RCHY1,*

361   *GBF1,* and the transcription factor *SHOX*, were key regulators identified in sub-networks of hub genes in

362   both analyses. These genes are involved in regulation of cell cycle, ECM, vesicular trafficking, immune

363   regulation, regulation of transcription and transduction, and biomineralization. They represent candidates

364   for further study.

365   Our analysis provides evidence of association of genic methylation repatterning with programmed

366   changes in phenotype. One interpretation of these outcomes is that dramatic shifts in gene expression are

367   accompanied by methylation changes that stabilize local chromatin to help reestablish homeostasis.

368   However, environmental changes also induce non-random changes in gene body methylation that influence

369   alternative splicing activity to modulate gene expression and phenotype (Ausin et al., 2012; Lev Maor et al.,

370   2015; Yang et al., 2014; Zhang et al., 2020). While our data do not specifically provide information on

371   regulation of gene expression, the integration of methylation and transcriptional information makes

372   significant inroads in the identification of networks underpinning coral phenotypic plasticity and provides a

373   roadmap for studies of other non-model organisms. As methylome repatterning is a signature of chromatin

374   reorganization and 3D architecture, integrating datasets enhances the potential to identify essential

375   interactions and likely signatures of gene-network coordination that may not be seen in DEG datasets alone

376   (Ouyang et al., 2020). Our integrated analyses offered the potential to predict phenotype at the gene-

377   network level and further postulate a light-mediated sequential response triggered by animal-sensing of

378   initial light stimulus to the change in skeletal morphology (**Fig. 6**).

379

380

Materials and Methods

Light exposure conditions

We first characterized the natural light exposure within colonies of the coral *Acropora palmata* by measuring the incident light on both upperside and underside surfaces of *in situ* branches (base, mid-branch, tips). We estimated the vertical attenuation coefficient (K_d) of the water column and retrieved daily irradiance cycles from SAMMO light sensors (Meteorological and Oceanographic Monitoring Academic Service at UNAM). Light measurements were taken with a cosine-corrected quantum sensor (Diving-PAM, Walz, Germany) previously calibrated against a manufacturer-calibrated quantum sensor (LI-1400, LI-COR, USA). We identified two daily integrated PAR (Photosynthetically Active Radiation) conditions for *in situ* colonies that we also used for the experimental setup: High Light (HL) surfaces represent fragments from upperside surfaces of branches exposed to ~20 mol quanta m^2 day^{-1} and Low Light (LL) surfaces represent fragments exposed to ~2 mol quanta m^2 day^{-1} (4-10% of upperside exposure).

Coral sample collection and experimental setup

To induce phenotypic plasticity, we performed a reciprocal transplant experiment in the reef-lagoon (30 m from the reef crest) in Puerto Morelos Reef National Park, Mexican Caribbean (**Fig 2A**). We sampled 3 colonies (representing 3 distinct multilocus genotypes, or genets, as detected with Standard Tools for Acroporid Genotyping STAGdb (Kitchen et al., 2020)) from a depth of 2-3 m (permits No. SGPA/DGVS/06960/17 and No. SGPA/DGVS/07846/17), each at least 300 m apart. We collected ~7 cm^2 fragments from HL (n= 42) and LL (n = 42) surfaces of branch surfaces keeping track of genet identification. We settled them in a reef-deployed PVC structure designed to simulate the light condition and colony position of source colonies.

We placed all coral fragments in their original light condition and orientation (*i.e.* HL facing up) and allowed them to heal and acclimate for 8 weeks (when new growth was observed). Subsequently, we

405   randomly divided HL fragments into control and treatment groups, equal grouping was done for LL

406   fragments. To induce phenotypic plasticity, coral fragments in treatment groups were flipped to the opposite

407   light condition and position (*i.e.* high light fragments were flipped to a low light condition, while LL fragments

408   were flipped to a HL position) (**Fig. 2A**). This second acclimatory period was carried out for 5+ weeks. We

409   estimated maximum excitation pressure over Photosystem II (Q_m=1 - [($\Delta F/F_m'$ at noon) / (F_v/F_m at dusk)]) to

410   determine successful acclimation to destination light condition (Iglesias-Prieto et al., 2004). We further

411   compared Q_m between experimental coral fragments (N=84) and *in situ* colonies (30 colonies, N=30

412   datapoints from upper and N=30 from underside surface of branches) (**Fig. S3A**).

413   Four group conditions were analyzed after 13+ weeks of experiment: HL controls (n= 21), HL→LL

414   treatments (High Light to Low Light, n = 21) LL controls (n= 21), LL→HL treatments (Low Light to High Light,

415   n = 21).

416   **Phenotype data analysis**

417   **Structural traits**

418   Phenotypic traits were measured based on parameters describing coral morphology and physiology

419   after 13+ weeks of experiment (**Table 1**). (n = 12 per group condition for non-invasive techniques, and n=9

420   per group condition for invasive techniques such as host total protein content, chlorophyll *a* content, and

421   symbiont cell counts) (**Fig. S1**). Morphological features were described by polyp density (number of polyps

422   per area) and by corallite height (mm), defined as the vertical distance between the corallite base and the

423   top of the theca. Corallite height was delineated into 'height classes' C_1 (0 - 1.5 mm), C_2 (>1.5 - 3 mm), and

424   C_3 (>3 mm) to further estimate polyp density at each height class. The projected area of each fragment was

425   estimated with photography and used to normalize physiological and morphological parameters.

426   To describe the structural and optical properties of the tissue we measured reflectance (*R*) of the intact

427   coral tissue as [De_{675} = log (1/R_{675})] and estimated absorbance at 675 nm (De_{675}) (Enríquez et al., 2005b;

428   Vásquez-Elizondo et al., 2017). In addition, we estimated symbiont density, Chlorophyll (Chl) *a* and *c* from

429   each fragment (Enríquez et al., 2005b; Iglesias-Prieto R. & Trench, 1994; Vásquez-Elizondo et al., 2017).

430   Briefly, tissue extractions were carried out using an air gun and filtered sea water (FSW). Slurries obtained

431   from this method were subsequently homogenized at low temperature (Tissue-Tearor Homogenizer

432   BioSpec Inc, USA) and centrifuged. The resulting pellet was re-suspended in filtered seawater and

433   preserved for symbiont cell counts (counted in a hemocytometer after the addition of 200 µl of iodine

434   preservation solution), and for Chl concentration (extracted with acetone/dimethyl sulfoxide 95:5 vol/vol).

435   Chl$a$ and c concentrations (ρ pigment content per projected surface area in mg Chl m^{-2}) were estimated

436   spectrophotometrically (3 reads per sample) with a modular spectrometer (Flame-T-UV-VIS, Ocean Optics

437   Inc., USA) using the equations described by Jeffrey and Humphrey (Jeffrey & Humphrey, 1975).

438   Downstream calculations of optical properties were performed integrating the parameters detailed

439   above (Enríquez et al., 2005b; Scheufen et al., 2017). Symbiont density and Chl$a$ were normalized to

440   calculate Chl$a$ per symbiont cell (Ci in pg Chl$a$ sym^{-1}). The specific absorption coefficient of Chl$a$ (a^{*}_{Chla}), a

441   descriptor of the light absorption efficiency of the holobiont, was estimated as [$a^{*}_{Chla}=(De_{675}/\rho)\cdot\ln(10)$]

442   (Enríquez et al., 2005b). Other calculations included the specific absorption coefficient of symbionts *in*

443   *hospite* (a^{*}_{sym}), a descriptor of the light absorption efficiency of symbionts. The host mass-specific efficiency

444   (a^{*}_{M}), a descriptor of the light absorption efficiency per host mass, a descriptor that quantifies the potential

445   benefits returned to the host, from the capacity of the symbiosis to collect solar energy.

446   **Physiological traits**

447   To estimate metabolic rates, we measured photosynthesis *in hospite* and estimated derived

448   parameters. Photosynthetic responses (Photosynthesis - Quantum Energy curves, PE curves) of coral

449   fragments were measured using a laboratory-made water-jacketed respirometer (Rodríguez-Román et al.,

450   2006). Corals were incubated in filtered sea water at a constant temperature (28 °C) and constant water

451   flow (generated by continuous agitation from magnetic stirrers). A Light Emitting Diode LED-system was

452   designed to enable automation of light increments every 10 minutes. Oxygen evolution was measured

453   continuously with a fiber-optic oxygen meter system (FireSting, Pyroscience) and the photosynthetic

454   efficiency (α), compensation irradiance (E_c), saturation irradiance (E_k), respiration rates (R_d), and maximum

455   photosynthetic rates (P_{max}), were calculated from the light-limited and light-saturated regions of the PE

456   curves (Iglesias-Prieto R. & Trench, 1994; Osinga et al., 2012). As a downstream calculation, the minimum

457   quantum requirement of photosynthesis (Φ^{-1}_{O2}) was estimated based on the linear regression of

458   photosynthetic rates during the light-limited region of PE curves. Φ^{-1}_{O2} is defined in terms of the light being

459   absorbed and used to drive photosynthesis or photosynthetic utilizable radiation (PUR). The ratio of

460   absorbed light is derived from previous measurements of reflectance [$A = 1- R$].

461   Similarities in phenotypic traits among the different group conditions and genets were analyzed with

462   non-metric multidimensional scaling (NMDS) ordination, plotted via Bray-Curtis dissimilarity matrix and 9999

463   permutations in vegan R-package. Statistical support for the NMDS clustering is provided by the

464   permutation-based hypothesis test analysis of similarities (ANOSIM) for experimental groups and for

465   genets.

466   **Coral tissue sampling and nucleic acid extraction**

467   After 13+ weeks of experiment (**Table 1**), coral tissue from each fragment (n = 12 per group condition)

468   was split into two samples and preserved, both in 95% ethanol and RNAlater (Ambion, Life Technology)

469   and stored at -80 ºC until processing.

470   Genomic DNA (gDNA) was extracted from 32 *A. palmata* fragments (n= 8 per group condition; 16

471   fragments per genet). We used the DNeasy Blood and Tissue Kit (Qiagen, Switzerland), as per the

472   manufacturer's protocol. gDNA concentration was quantified at 0.5-1.5 μg (Qubit® dsDNA BR Assay Kit on

473   a Qubit® 2.0. Fluorometer) and sent for Whole Genome Bisulfite Sequencing (WGBS) at Admera Health

474   (New Jersey, USA).

475   Total RNA was extracted from the same 32 *A. palmata* fragments used in WGBS as previously noted.

476   The tissue from each fragment was homogenized in TRIzol reagent (Ambion, Life Technology) before

477   centrifugation with chloroform for 15 minutes at 12,000 x g at 4 ºC. The aqueous phase was then isolated

478   and cleaned using Qiagen RNeasy Mini kit (Qiagen), as per the manufacturer's protocol with an additional

479   on-column DNase treatment using RNase-Free DNase Set (Qiagen). To maximize concentration of eluted

480   RNA, the same 35 μl of RNAse-free water was twice passed through the spin column for the final isolation

481   step. Concentration and purity ($A_{260/280}$) were analyzed via NanoDrop ND-1000 spectrometer and quality

482   assessed (RIN > 7) with Agilent 2100 Bioanalyzer (Agilent Technologies). Total RNA was sent to Admera

483   Health (New Jersey, USA) where concentration and purity was re-analyzed (Qubit® dsDNA BR Assay Kit

484   on a Qubit® 2.0. Fluorometer).

485   **Methylome sequencing and data processing**

486   Sequencing libraries were prepared with an average sequencing library insert size of 450 bp and

487   according to TruSeq® DNA Methylation Kit protocol, Sample Preparation Guide (Illumina Inc., USA). Briefly,

488   standard reaction mix consisting of 130 µl of the CT Conversion Reagent and 20 µl of each DNA sample

489   were used for bisulfite conversion (EZ DNA Methylation-Gold™ Kit) in a thermal cycler (Eppendorf®

490   Mastercycler® Pro S). After the incubation period, bisulfite converted DNA was purified following the

491   protocol of EZ DNA Methylation-Gold™ Kit. The bisulfite converted sequencing library was enriched

492   following the TruSeq® DNA Methylation Kit protocol. Libraries were validated and quantified with qPCR.

493   Sequencing was performed in Illumina Hi-Seq platform with pair-end reads of 2x150 and a mean depth

494   coverage of 30x (Illumina Inc., USA). The estimated number of passed filter reads per sample was 110-120

495   million paired-end reads (55-60M reads in each direction).

496   The expected bisulfate conversion efficiency for this method is >99%. While Lambda DNA was not

497   spiked-in to estimate non-conversion and mis-sequencing rate, we can assume that only CpG methylation

498   context occurs in corals (Liew et al., 2018a; Trigg et al., 2022), hence, non-CpG methylation should be close

499   to zero. We detected an average of 13.96% (SE=0.07) methylation in CpG context and an insignificant

500   0.54% (SE = 0.01) in non-CpG contexts (CHG and CHH, where H is A, T, or C), which resulted in an inferred

501   bisulfite conversion efficiency of ~99.5%.

502   **Data processing.** Methylation analysis was performed using Bismark 020.0 (Krueger and Andrews,

503   2011). Briefly (**Fig. S2**), FASTQ files were quality-filtered, and adapter sequences trimmed using Trim

504   Galore 0.5.0 (Krueger, 2018). A bisulfite-converted reference genome file was generated using Bismark-

505   Bowtie2 algorithm, and the epigenome library sequenced data was aligned to the *Acropora palmata* genome

(JAOVVL01). Methylation information was then extracted from the output SAM files and resulting genome tracks were used for the visualization and reporting of downstream differential methylation calculations. Methylated and unmethylated read counts for all cytosines across the genome in the CG, CHG, and CHH context were obtained from census files.

The approach used for downstream analysis was based on the identification of Differentially Methylated Positions (DMPs) and Differentially Methylated Genes (DMGs) using R package Methyl-IT 0.3.1.2 (Sanchez et al., 2019; Sanchez & Mackenzie, 2020; Yang et al., 2020) (**Fig. S2**). Briefly, methylation count (COV) files were read into R to calculate Hellinger Divergence (*HD*, a variable used to measure methylation level divergence) by using the pool of methylation counts for control samples as reference. Potential DMPs (pDMPs) were estimated based on critical values of $HD_{\alpha=0.05}$ for each sample from the best fitted probability distribution model; in this case, a 3-parameter gamma distribution model. Final DMPs were estimated from the set of pDMPs by calculating the optimal cutoff threshold for *HD* based on Youden index. Generalized linear regression analysis (generalized linear model, GLM) was applied to test the difference between group DMP counts (among control and treatment groups; HL vs HL→LL, LL vs LL→HL) for selected genomic features. The fitting algorithm approaches provided by glm and glm.nb functions from the R packages stat and MASS were used for Poisson (PR), Quasi-Poisson (QPR) and Negative Binomial (NBR) models with logarithmic link. The '*countTest2*' function in Methyl-IT was used to implement the selected model. The following parameters were applied to identify significant DMGs (Yang et al., 2020): 1) the minimum DMP count per bp on gene-body: *CountPerBp* = 2.5; 2) a minimum count per sample (on average) in at least 5 DMPs in one group: *minCountPerIndv* = 5; 3) a maximum coefficient of variance for each group: *maxGrpCV* = 1, 4) minimum value of the logarithm of fold-changes: *Minlog2FC* ≤ 1; 5) *p*-value cutoff: *pvalCutOff* = 0.01, 6) *p*-value adjustment was performed by Benjamini & Hochberg method: *pAdjustMethod* = "BH". Parameters 1 to 3 are addressed to prevent spurious DMGs, which cannot be rejected by the generalized linear regression algorithms.

Genes overcoming constraints 1 to 5 and displaying significant difference between control and treatment comparison according to likelihood ratio test (LRT) derived by the *anova* function from stats

532   packages were identified as DMGs (**Fig. S2**). A detailed description of how to define and compute DMPs

533   and potential DMGs is included in the Methyl-IT vignettes and the package manual, available at

534   https://github.com/genomaths/MethylIT. *Acropora palmata* genome annotation file

535   Apalm_assembly_v2.0_180910.gff3 was used to annotate genome features.

536   **Methyl-IT downstream analysis (Methyl-IT.utils**). A Hierarchical clustering (HC) was performed to

537   provide an initial estimation of the number of possible groups and information on their members. The

538   effectivity of HC depends on the experimental dataset, the metric used, and the glomeration algorithm

539   applied. Ward's agglomeration algorithm was used as it performs much better on biological experimental

540   datasets than the other of the available algorithms (e.g. UPGMA, UPGMC).

541   **RNA sequencing and data processing**

542   RNA libraries for 2x150bp paired-end sequencing were prepared using the NEBNext Ultra II

543   Nondirectional Library Prep Kit with polyA selection (New England Biolabs, Inc.). Samples were run on one

544   plate of the Illumina NovaSeq platform. Illumina universal adapters and reads below PHRED of 22 were

545   trimmed using Cutadapt(Martin, 2011). Filtered reads were mapped to the *Acropora palmata* genome

546   (JAOVVL01) using the RNA-seq aligner STAR (2.5.3a) with read count data generated by the –quantMode

547   GeneCount parameter. Reads were verified using the generated BAM files for input into htseq-count.

548   **Differential gene expression analysis.** Gene count normalization and differential expression

549   analysis was performed using DESeq2 3.12.0. Significant Differentially Expressed Genes (DEGs) were

550   determined via pairwise comparison among control and treatment groups (HL vs HL→LL, LL vs LL→HL)

551   and genet, with a false discovery rate-adjusted P value (FDR) of < 0.05 (**Fig. S2**).

552   **Network-associated responses**

553   A network provides a collection of nodes and edges that represent our system of elements (genes)

554   interacting or regulating each other (Albert, 2005). Based on available data, we chose gene-gene interaction

555   networks (predicted protein-protein interaction networks), as they are undirected, and the graph is non-

556   sequential (X affects Y, but we do not know how) (Le Novere, 2015). A key feature for the biological

557   interpretation of graph properties are hubs. Small-degree nodes (with small number of interactions) are the

558   most abundant, but high-degree nodes or hubs, although less frequent, have a much higher number of

559   interactions (Dennison & Alberte, 1982). In this context, the likelihood that a gene is essential correlates

560   with the number of interactions, and random node disruption will not lead to major losses of connectivity. In

561   contrast, the loss of hubs will cause a major breakdown of the network (Albert, 2005; Jeong et al., 2001;

562   Said et al., 2004).

563   **Agnostic biological network analysis: Network-based integration of DMG and DEG datasets**

564   (**Fig. S2**)**.**

565   To understand the interaction between the change in methylomes (n = 32) and transcriptomes (n =

566   32), and how genes contributed to the change in phenotype, we performed a Weighted Gene Correlation

567   Network Analysis (WGCNA 1.71) (Langfelder & Horvath, 2008). We generated a dataset (gene list)

568   comprising the subsets of 1) all DMGs (from Methyl-IT 0.3.1.2) and 2) DEGs (from DESeq2 3.12.0) that

569   presented at least one DMP (from Methyl-IT 0.3.1.2) after the change in light treatment. This dataset

570   included outputs from all groups (HL, HL→LL, LL, LL→HL) and genets to discover general patterns of gene

571   contribution. Additionally, a binary annotation was included to keep track of DMG, DEG and both DMG-

572   DEG. As a results, each sample was represented as vector of 3272 genes/coordinates, where each

573   coordinate was given by the sum of *HD* at each DMP on the given gene.

574   We first performed a hierarchical clustering (HC) applying Ward's agglomeration algorithm to provide

575   an initial estimation of the number of possible groups and information on their members. Methyl-IT function

576   *pcaLDA* was used to perform a Principal Component Analysis (PCA) and a PCA + Linear Discriminant

577   Analysis (LDA). Unlike hierarchical clustering (HC) and PCA, LDA is a supervised machine learning

578   approach, therefore, we must provide a prior classification of the samples, which can be derived, for

579   example, from the HC, or from a previous exploratory analysis with PCA. Based on the cumulative

580   proportion of variance, the PC1 and PC2 carried 92% of the total sample variance and could split the

581   samples into meaningful groups. We saved the loadings from each gene. Loadings are coefficients in linear

582 combination predicting a variable by the (standardized) components. The sum of loading squares within

583 each component are the eigenvalues (components' variances), which is 1 for standardized loadings. In

584 other words, loadings are "standard deviations" and the square of the loading of gene "A" quantitatively

585 expresses the percent of the PC variance carried by gene "A". PC-scores for each gene indicate the

586 discriminatory power in the clustering (control vs treatment) and its genomic/epigenomic contribution (in

587 terms of proportion of the whole phenotypic variance) to the change in phenotype.

588 Genes PC-scores (gene-score) from 14 PCs were then used to build the pairwise correlation matrix

589 for the WGCNA. Kendal's tau correlation was selected since it is better at detecting nonlinear behaviors and

590 is more conservative than Pearson's correlation. The resulting weighted correlation matrix was then

591 constructed as a network in the R-package WGCNA (Langfelder & Horvath, 2008) and exported as edge

592 list (interactions with weights) and node list files with assigned modules into Cytoscape 3.8.2 for

593 visualization. Each entity of the dataset is a (gene) node, and 2 nodes are connected if their correlation or

594 distance reach a threshold (here set to 0.4). Network topology included gene discriminatory power (gene-

595 scores) and a measure of how similarly they contributed to this classification (weight from correlation). The

596 correlation network was analyzed and visualized in Cytoscape 3.8.2 (Sanchez & Mackenzie, 2020).

597 **Predicted biological networks: network-associated responses from DMGs** (**Fig. S2**)**.** To identify

598 the biological meaning of potential relationships among DMGs we inferred gene interaction networks from

599 *stringApp* in Cytoscape 3.8.2. The associations in the *string* database provides known and predicted

600 protein−protein associations data for many organisms, including both physical interactions and functional

601 associations, by integrating available experimental data and pathways from curated databases (Doncheva

602 et al., 2019; Szklarczyk et al., 2017). We used only our detected DMGs (without network expansion) as

603 input in *string protein query* (Swiss-Prot hit name) to retrieve an arbitrary long list of nodes and interactions.

604 This approach is generally used to retrieve string networks from proteomics and transcriptomics studies

605 (Doncheva et al., 2019; Szklarczyk et al., 2017) .

606 The best hit for baseline networks was reached with *string query* for *Homo sapiens*. We recognize that

607 cross-species knowledge transfer is quite challenging because the phylum cnidaria diverged from Bilateria

608   550 million years ago and may have fundamentally different genetic architectures. Also, as species diverge,

609   protein functions change and are re-purposed through divergent and convergent evolution, and genetic

610   interactions are often rewired (Fan et al., 2019). Parallel to this, in network-based approaches most

611   predicted interactions for each species are not experimentally verified. Despite these limitations, the best

612   hit in *string query* was still *Homo sapiens*, perhaps, due to the presence of conserved stress response,

613   conserved pathways (*e.g.* extrinsic and intrinsic apoptotic pathways, ion trafficking system) and (predicted)

614   gene products between early and late branching metazoans at the molecular level (Bhattacharya et al.,

615   2016; Courtial et al., 2017; Davy et al., 2012; Drake et al., 2013; Ottaviani et al., 2020). Furthermore, genes

616   that emerged from our data and clustering analyses predicted gene interactions associated to coral

617   biological processes that aligned well to the measured phenotypes, suggesting our analytical approach was

618   plausible.

619   The retrieved baseline network was then analysed statistically incorporating extended centrality

620   measures from CentiScape 2.2 App (EigenVector of centrality). We chose Eigenvector centrality because

621   this attribute ranks nodes by taking into consideration not only the number of interactions of a node (degree),

622   but also, the centrality of the interactions that it is connected to. In other words, a node is important if it is

623   interacting with other important nodes. The output dataset generated from Methyl-IT 0.3.1.2 was imported

624   into this network to assign node attributes.

625   To identify hub genes, we assigned methylation signal and Eigenvector of centrality as attributes to

626   the nodes (Sanchez & Mackenzie, 2020). In networks, a protein with a very high Eigenvector is a protein

627   interacting with several important proteins (regulating them or being regulated by them), thus suggesting a

628   central super-regulatory role or a critical target of a regulatory pathway. We used Eigenvector as parameter

629   to perform k-means clustering algorithm (*clusterMakerApp* in Cytoscape 3.8.2.) (Sanchez & Mackenzie,

630   2020) to identify clusters of hub genes. To identify over-represented functions in the large set of DMGs, we

631   performed Network Enrichment Analysis (NEA). Enriched terms were retrieved as UniProt KnowledgeBase

632   (kw) categories in String Enrichment App in Cytoscape 3.8.2 (Sanchez & Mackenzie, 2020).

633   **Predicted biological networks: Network-associated responses from DEGs**. To identify the

634   biological meaning of potential relationships among DEGs we inferred gene interaction networks from

635   *stringApp* in Cytoscape 3.8.2 with the same workflow as for DMGs interaction networks. The output dataset

636   generated in DESeq2 3.12.0 was imported to this baseline network to assign gene regulation (up-regulated

637   or down-regulated) as a node attribute.

638   **Predicted biological networks: Network-based integration of DMG and DEG datasets.**

639   To further explore the association between DMGs and DEGs, we integrated DEGs to DMGs network

640   data sets. The integration was done at the cluster level (after *clusterMakerApp* independent analyses) with

641   the criteria that a DEG-cluster be selected if it contained at least one gene also identified as DMG. The

642   output datasets generated from Methyl-IT 0.3.1.2 and DESeq2 3.12.0 were imported to this baseline

643   network to assign node attributes. With this approach we were able to enhance networks by adding new

644   attributes to the nodes: DMG, DEG, both DMG-DEG. We maintained the attributes Eigenvector of centrality,

645   methylation signal (from Methyl-IT 0.3.1.2), and gene regulation (upregulated or downregulated from

646   DESeq2 3.12.0). A new clustering was performed based of Eigenvector of centrality ranks and 1st, 2nd and

647   3rd neighbours of high ranked nodes. To identify over-represented functions in the DMGs-DEGs integrated

648   clusters, we performed a Network Enrichment Analysis (NEA) to each new cluster. Enriched terms were

649   retrieved as UniProt KnowledgeBase categories (kw) in String Enrichment App (Sanchez & Mackenzie,

650   2020). Because key coral biological processes emerged from the new clustering, we further explored

651   potential key regulators and candidate genes involved in light-mediated phenotypic plasticity of structural

652   traits in corals.

653

654   **Acknowledgments**

655

668

669   **References**
670
671   Albert, R. (2005). Scale-free networks in cell biology. In *Journal of Cell Science* (Vol. 118, Issue
672   21, pp. 4947–4957). The Company of Biologists. https://doi.org/10.1242/jcs.02714
673   Allemand, D., Tambutté, É., Girard, J. P., & Jaubert, J. (1998). Organic matrix synthesis in the
674   scleractinian coral Stylophora pistillata: Role in biomineralization and potential target of the
675   organotin tributyltin. *Journal of Experimental Biology*, *201*(13), 2001–2009.
676   https://doi.org/10.1242/jeb.201.13.2001
677   Ausin, I., Greenberg, M. V. C., Li, C. F., & Jacobsen, S. E. (2012). The splicing factor SR45
678   affects the RNA-directed DNA methylation pathway in Arabidopsis. *Epigenetics*, *7*(1), 29–
679   33. https://doi.org/10.4161/epi.7.1.18782
680   Baums, I. B., Devlin-Durante, M. K., & LaJeunesse, T. C. (2014). New insights into the
681   dynamics between reef corals and their associated dinoflagellate endosymbionts from
682   population genetic studies. *Molecular Ecology*, *23*(17), 4203–4215.
683   https://doi.org/10.1111/MEC.12788
684   Baums, I. B., Miller, M. W., & Hellberg, M. E. (2006). Geographic variation in clonal structure
685   in a reef-building Caribbean coral, Acropora palmata. *Ecological Monographs*, *76*(4), 503–
686   519. https://doi.org/1doi.org/10.1890/0012-9615(2006)076[0503:GVICSI]2.0.CO;2
687   Bhattacharya, D., Agrawal, S., Aranda, M., Baumgarten, S., Belcaid, M., Drake, J. L., Erwin, D.,
688   Foret, S., Gates, R. D., Gruber, D. F., Kamel, B., Lesser, M. P., Levy, O., Liew, Y. J.,
689   MacManes, M., Mass, T., Medina, M., Mehr, S., Meyer, E., … Falkowski, P. G. (2016).
690   Comparative genomics explains the evolutionary success of reef-forming corals. *ELife*,
691   *5*(MAY2016), 1–26. https://doi.org/10.7554/eLife.13288
692   Borges, R. (2008). Plasticity comparisons between plants and animals. *Plant Signaling and*
693   *Behavior*, *3*(6), 367–375.
694   https://doi.org/https://www.ncbi.nlm.nih.gov/pmc/articles/PMC2634305/pdf/psb0306_0367.
695   pdf

696   Bossdorf, O., Arcuri, D., Richards, C. L., & Pigliucci, M. (2010). Experimental alteration of
697   DNA methylation affects the phenotypic plasticity of ecologically relevant traits in
698   Arabidopsis thaliana. *Evolutionary Ecology*, *24*(3), 541–553.
699   https://doi.org/10.1007/s10682-010-9372-7
700   Buitrago, D., Labrador, M., Arcon, J. P., Lema, R., Flores, O., Esteve-Codina, A., Blanc, J.,
701   Villegas, N., Bellido, D., Gut, M., Dans, P. D., Heath, S. C., Gut, I. G., Brun Heath, I., &
702   Orozco, M. (2021). Impact of DNA methylation on 3D genome structure. *Nature*
703   *Communications*, *12*(1). https://doi.org/10.1038/s41467-021-23142-8
704   Chevin, L. M., Lande, R., & Mace, G. M. (2010). Adaptation, plasticity, and extinction in a
705   changing environment: Towards a predictive theory. *PLoS Biology*, *8*(4), e1000357.
706   https://doi.org/10.1371/journal.pbio.1000357
707   Cohen, I., Dubinsky, Z., & Erez, J. (2016). Light enhanced calcification in hermatypic corals:
708   New insights from light spectral responses. *Frontiers in Marine Science*, *2*(JAN).
709   https://doi.org/10.3389/fmars.2015.00122
710   Courtial, L., Picco, V., Grover, R., Cormerais, Y., Rottier, C., Labbe, A., Pagès, G., & Ferrier-
711   Pagès, C. (2017). The c-Jun N-Terminal kinase prevents oxidative stress induced by UV and
712   thermal stresses in corals and human cells. *Scientific Reports*, *7*(April), 1–10.
713   https://doi.org/10.1038/srep45713
714   Davy, S. K., Allemand, D., & Weis, V. M. (2012). Cell Biology of Cnidarian-Dinoflagellate
715   Symbiosis. *Microbiology and Molecular Biology Reviews*, *76*(2), 229–261.
716   https://doi.org/10.1128/mmbr.05014-11
717   De Kroon, H., Huber, H., Stuefer, J. F., & Van Groenendael, J. M. (2005). A modular concept of
718   phenotypic plasticity in plants. In *New Phytologist* (Vol. 166, Issue 1, pp. 73–82).
719   https://doi.org/10.1111/j.1469-8137.2004.01310.x
720   Dennison, W. C., & Alberte, R. S. (1982). Photosynthetic Responses of Zostera marina L.
721   (Eelgrass) to in situ Manipulations of Light Intensity. *Oecologia*, *55*, 137–144.
722   Dimond, J. L., Gamblewood, S. K., & Roberts, S. B. (2017). Genetic and epigenetic insight into
723   morphospecies in a reef coral. *Molecular Ecology*, *26*(19), 5031–5042.
724   https://doi.org/10.1111/mec.14252
725   Dimond, J. L., & Roberts, S. B. (2016). Germline DNA methylation in reef corals: Patterns and
726   potential roles in response to environmental change. *Molecular Ecology*, *25*(8), 1895–1904.
727   https://doi.org/10.1111/mec.13414
728   Dixon, G., Liao, Y., Bay, L. K., & Matz, M. V. (2018). Role of gene body methylation in
729   acclimatization and adaptation in a basal metazoan. *Proceedings of the National Academy of*
730   *Sciences of the United States of America*, *115*(52), 13342–13346.
731   https://doi.org/10.1073/pnas.1813749115
732   Doncheva, N. T., Morris, J. H., Gorodkin, J., & Jensen, L. J. (2019). Cytoscape StringApp:
733   Network Analysis and Visualization of Proteomics Data. *Journal of Proteome Research*,
734   *18*(2), 623–632. https://doi.org/10.1021/acs.jproteome.8b00702
735   Drake, J. L., Mass, T., Haramaty, L., Zelzion, E., Bhattacharya, D., & Falkowski, P. G. (2013).
736   Proteomic analysis of skeletal organic matrix from the stony coral Stylophora pistillata.
737   *Proceedings of the National Academy of Sciences of the United States of America*, *110*(10),
738   3788–3793. https://doi.org/10.1073/pnas.1301419110

739 Durante, M. K., Baums, I. B., Williams, D. E., Vohsen, S., & Kemp, D. W. (2019). What drives
740   phenotypic divergence among coral clonemates of Acropora palmata? *Molecular Ecology*,
741   *28*(13), 3208–3224. https://doi.org/10.1111/mec.15140
742 Enríquez, S., Méndez, E. R., Hoegh-Guldberg, O., & Iglesias-Prieto, R. (2017). Key functional
743   role of the optical properties of coral skeletons in coral ecology and evolution. *Proceedings*
744   *of the Royal Society B: Biological Sciences*, *284*(1853), 20161667.
745   https://doi.org/10.1098/rspb.2016.1667
746 Enríquez, S., Méndez, E. R., & Iglesias-Prieto, R. (2005a). Multiple scattering on coral skeletons
747   enhances light absorption by symbiotic algae. *Limnology and Oceanography*, *50*(4), 1025–
748   1032. https://doi.org/10.4319/lo.2005.50.4.1025
749 Enríquez, S., Méndez, E. R., & Iglesias-Prieto, R. (2005b). Multiple scattering on coral skeletons
750   enhances light absorption by symbiotic algae. *Limnology and Oceanography*, *50*(4), 1025–
751   1032. https://doi.org/10.4319/lo.2005.50.4.1025
752 Falkowski, P. G., Dubinsky, Z., Muscatine, L., & Porter, J. W. (1984). Light and the
753   Bioenergetics of a Symbiotic Coral. *BioScience*, *34*(11), 705–709.
754   https://doi.org/10.2307/1309663
755 Falkowski, P. G., Dubinsky, Z., & Wyman, K. (1985). Growth-irradiance relationships in
756   phytoplankton. *Limnology and Oceanography*, *30*(2), 311–321.
757 Fan, J., Cannistra, A., Fried, I., Lim, T., Schaffner, T., Crovella, M., Hescott, B., & Leiserson, M.
758   D. M. (2019). Functional protein representations from biological networks enable diverse
759   cross-species inference. *Nucleic Acids Research*, *47*(9), 1–13.
760   https://doi.org/10.1093/nar/gkz132
761 Gattuso, J. P., Allemand, D., & Frankignoulle, M. (1999). Photosynthesis and calcification at
762   cellular, organismal and community levels in coral reefs: A review on interactions and
763   control by carbonate chemistry. *American Zoologist*, *39*(1), 160–183.
764   https://doi.org/10.1093/icb/39.1.160
765 Gutner-Hoch, E., Ben-Asher, H. W., Yam, R., Shemesh, A., & Levy, O. (2017). Identifying
766   genes and regulatory pathways associated with the scleractinian coral calcification process.
767   *PeerJ*, *2017*(7), 3590. https://doi.org/10.7717/peerj.3590
768 Hafner, A., & Mackenzie, S. (2023). Re-analysis of publicly available methylomes using signal
769   detection yields new information. *Scientific Reports*, *13*(1), 3307.
770   https://doi.org/10.1038/s41598-023-30422-4
771 Hashimshony, T., Zhang, J., Keshet, I., Bustin, M., & Cedar, H. (2003). The role of DNA
772   methylation in setting up chromatin structure during development. In *NATURE GENETICS*
773   (Vol. 34, Issue 2). http://www.nature.com/naturegenetics
774 Hemond, E. M., Kaluziak, S. T., & Vollmer, S. V. (2014). The genetics of colony form and
775   function in Caribbean Acropora corals. *BMC Genomics*, *15*(1).
776   https://doi.org/10.1186/1471-2164-15-1133
777 Huck-Hui, N., & Bird, A. (1999). DNA methylation and chromatin modification. *Current*
778   *Opinion in Genetics and Development*, *9*(2), 158–163. https://doi.org/10.1016/S0959-
779   437X(99)80024-0
780 Iglesias-Prieto, R., Beltrán, V. H., LaJeunesse, T. C., Reyes-Bonilla, H., & Thomé, P. E. (2004).
781   Different algal symbionts explain the vertical distribution of dominant reef corals in the
782   eastern Pacific. *Proceedings of the Royal Society B: Biological Sciences*, *271*(1549), 1757–
783   1763. https://doi.org/10.1098/rspb.2004.2757

784 Iglesias-Prieto R., & Trench, R. K. (1994). Acclimation and adaptation to irradiance in symbiotic
785   dinoflagellates. 1.Responses of the photosynthetic unit to changes in photon flux density.
786   *Marine Ecology Progress Series*, *113*(1–2), 163–176. https://doi.org/10.3354/meps113163
787 Jeffrey, S. W., & Humphrey, G. F. (1975). New spectrophotometric equations for determining
788   chlorophylls a, b, c1 and c2 in higher plants, algae and natural phytoplankton. *Biochemie*
789   *Und Physiologie Der Pflanzen*, *167*(2), 191–194. https://doi.org/10.1016/s0015-
790   3796(17)30778-3
791 Jeong, H., Mason, S. P., Barabási, A. L., & Oltvai, Z. N. (2001). Lethality and centrality in
792   protein networks. *Nature*, *411*(6833), 41–42. https://doi.org/10.1038/35075138
793 Kemp, D. W., Thornhill, D. J., Rotjan, R. D., Iglesias-Prieto, R., Fitt, W. K., & Schmidt, G. W.
794   (2015). Spatially distinct and regionally endemic Symbiodinium assemblages in the
795   threatened Caribbean reef-building coral Orbicella faveolata. *Coral Reefs*, *34*(2), 535–547.
796   https://doi.org/10.1007/s00338-015-1277-z
797 Kitchen, S. A., Von Kuster, G., Kuntz, K. L. V., Reich, H. G., Miller, W., Griffin, S., Fogarty, N.
798   D., & Baums, I. B. (2020). STAGdb: a 30K SNP genotyping array and Science Gateway for
799   Acropora corals and their dinoflagellate symbionts. *Scientific Reports*, *10*(1), 1–18.
800   https://doi.org/10.1038/s41598-020-69101-z
801 Kozmik, Z., Ruzickova, J., Jonasova, K., Matsumoto, Y., Vopalensky, P., Kozmikova, I., Strnad,
802   H., Kawamura, S., Piatigorsky, J., Paces, V., & Vlcek, C. (2008). Assembly of the cnidarian
803   camera-type eye from vertebrate-like components. *Proceedings of the National Academy of*
804   *Sciences of the United States of America*, *105*(26), 8989–8993.
805   https://doi.org/10.1073/pnas.0800388105
806 Kundariya, H., Sanchez, R., Yang, X., Hafner, A., & Mackenzie, S. A. (2022). Methylome
807   decoding of RdDM-mediated reprogramming effects in the Arabidopsis MSH1 system.
808   *Genome Biology*, *23*(1). https://doi.org/10.1186/s13059-022-02731-w
809 LaJeunesse, T. C., Parkinson, J. E., Gabrielson, P. W., Jeong, H. J., Reimer, J. D., Voolstra, C.
810   R., & Santos, S. R. (2018). Systematic Revision of Symbiodiniaceae Highlights the
811   Antiquity and Diversity of Coral Endosymbionts. *Current Biology*, *28*(16), 2570-2580.e6.
812   https://doi.org/10.1016/j.cub.2018.07.008
813 Langfelder, P., & Horvath, S. (2008). WGCNA: An R package for weighted correlation network
814   analysis. *BMC Bioinformatics*, *9*. https://doi.org/10.1186/1471-2105-9-559
815 Le Novere, N. (2015). Quantitative and logic modelling of molecular and gene networks. In
816   *Nature Reviews Genetics* (Vol. 16, Issue 3, pp. 146–158). https://doi.org/10.1038/nrg3885
817 Lev Maor, G., Yearim, A., & Ast, G. (2015). The alternative role of DNA methylation in splicing
818   regulation. In *Trends in Genetics* (Vol. 31, Issue 5).
819   https://doi.org/10.1016/j.tig.2015.03.002
820 Liew, Y. J., Zoccola, D., Li, Y., Tambutté, E., Venn, A. A., Michell, C. T., Cui, G., Deutekom, E.
821   S., Kaandorp, J. A., Voolstra, C. R., Forêt, S., Allemand, D., Tambutté, S., & Aranda, M.
822   (2018a). Epigenome-associated phenotypic acclimatization to ocean acidification in a reef-
823   building coral. *Science Advances*, *4*(6), eaar8028. https://doi.org/10.1126/sciadv.aar8028
824 Liew, Y. J., Zoccola, D., Li, Y., Tambutté, E., Venn, A. A., Michell, C. T., Cui, G., Deutekom, E.
825   S., Kaandorp, J. A., Voolstra, C. R., Forêt, S., Allemand, D., Tambutté, S., & Aranda, M.
826   (2018b). Epigenome-associated phenotypic acclimatization to ocean acidification in a reef-
827   building coral. *Science Advances*, *4*(6), eaar8028. https://doi.org/10.1126/sciadv.aar8028

828 Malik, A., Einbinder, S., Martinez, S., Tchernov, D., Haviv, S., Almuly, R., Zaslansky, P.,
829   Polishchuk, I., Pokroy, B., Stolarski, J., & Mass, T. (2021). Molecular and skeletal
830   fingerprints of scleractinian coral biomineralization: From the sea surface to mesophotic
831   depths. *Acta Biomaterialia*, *120*, 263–276. https://doi.org/10.1016/j.actbio.2020.01.010
832 Martin, M. (2011). Cutadapt removes adapter sequences from high-throughput sequencing reads.
833   *EMBnet.Journal*, *17*(1), 10. https://doi.org/10.14806/ej.17.1.200
834 Mummadisetti, M. P., Drake, J. L., & Falkowski, P. G. (2021). The spatial network of skeletal
835   proteins in a stony coral. *Journal of the Royal Society Interface*, *18*(175).
836   https://doi.org/10.1098/rsif.2020.0859
837 Nicotra, A. B., Atkin, O. K., Bonser, S. P., Davidson, A. M., Finnegan, E. J., Mathesius, U., Poot,
838   P., Purugganan, M. D., Richards, C. L., Valladares, F., & van Kleunen, M. (2010). Plant
839   phenotypic plasticity in a changing climate. *Trends in Plant Science*, *15*(12), 684–692.
840   https://doi.org/10.1016/j.tplants.2010.09.008
841 Osinga, R., Iglesias-Prieto, R., & Enriquez, S. (2012). Measuring Photosynthesis in Symbiotic
842   Invertebrates: A Review of Methodologies, Rates and Processes. *Applied Photosynthesis*.
843   https://doi.org/10.5772/29339
844 Ottaviani, A., Eid, R., Zoccola, D., Pousse, M., Dubal, J. M., Barajas, E., Jamet, K., Lebrigand,
845   K., Lapébie, P., Baudoin, C., Giraud-Panis, M. J., Rouan, A., Beauchef, G., Guéré, C., Vié,
846   K., Barbry, P., Tambutté, S., Gilson, E., & Allemand, D. (2020). Longevity strategies in
847   response to light in the reef coral Stylophora pistillata. *Scientific Reports*, *10*(1), 1–10.
848   https://doi.org/10.1038/s41598-020-76925-2
849 Ouyang, W., Cao, Z., Xiong, D., Li, G., & Li, X. (2020). Decoding the plant genome: From
850   epigenome to 3D organization. *Journal of Genetics and Genomics*, *47*(8), 425–435.
851   https://doi.org/10.1016/j.jgg.2020.06.007
852 Ow, Y. X., & Todd, P. A. (2010). Light-induced morphological plasticity in the scleractinian
853   coral Goniastrea pectinata and its functional significance. *Coral Reefs*, *29*(3), 797–808.
854   https://doi.org/10.1007/s00338-010-0631-4
855 Pelizzola, M., & Ecker, J. R. (2011). The DNA methylome. *FEBS Letters*, *585*(13), 1994–2000.
856   https://doi.org/10.1016/j.febslet.2010.10.061
857 Putnam, H. M., Davidson, J. M., & Gates, R. D. (2016). Ocean acidification influences host DNA
858   methylation and phenotypic plasticity in environmentally susceptible corals. *Evolutionary*
859   *Applications*, *9*(9), 1165–1178. https://doi.org/10.1111/eva.12408
860 Roberts, S. B., & Gavery, M. R. (2012). Is there a relationship between DNA methylation and
861   phenotypic plasticity in invertebrates? *Frontiers in Physiology*, *2 JAN*, 116.
862   https://doi.org/10.3389/fphys.2011.00116
863 Rodríguez-Casariego, J. A., Mercado-Molina, A. E., Garcia-Souto, D., Ortiz-Rivera, I. M.,
864   Lopes, C., Baums, I. B., Sabat, A. M., & Eirin-Lopez, J. M. (2020). Genome-Wide DNA
865   Methylation Analysis Reveals a Conserved Epigenetic Response to Seasonal Environmental
866   Variation in the Staghorn Coral Acropora cervicornis. *Frontiers in Marine Science*, *7*, 822.
867   https://doi.org/10.3389/fmars.2020.560424
868 Rodríguez-Román, A., Hernández-Pech, X., Thomé, P. E., Enríquez, S., & Iglesias-Prieto, R.
869   (2006). Photosynthesis and light utilization in the Caribbean coral Montastraea faveolata
870   recovering from a bleaching event. *Limnology and Oceanography*, *51*(6), 2702–2710.
871   https://doi.org/10.4319/lo.2006.51.6.2702

872 Said, M. R., Begley, T. J., Oppenheim, A. V., Lauffenburger, D. A., & Samson, L. D. (2004).
873   Global network analysis of phenotypic effects: Protein networks and toxicity modulation in
874   Saccharomyces cerevisiae. *Proceedings of the National Academy of Sciences of the United*
875   *States of America*, *101*(52), 18006–18011. https://doi.org/10.1073/pnas.0405996101

876 Sanchez, R., & Mackenzie, S. A. (2016a). Genome-wide discriminatory information patterns of
877   cytosine DNA methylation. *International Journal of Molecular Sciences*, *17*(6), 938.
878   https://doi.org/10.3390/ijms17060938

879 Sanchez, R., & Mackenzie, S. A. (2016b). Information thermodynamics of cytosine DNA
880   methylation. *PLoS ONE*, *11*(3). https://doi.org/10.1371/journal.pone.0150427

881 Sanchez, R., & Mackenzie, S. A. (2020). Integrative Network Analysis of Differentially
882   Methylated and Expressed Genes for Biomarker Identification in Leukemia. *Scientific*
883   *Reports*, *10*(1), 1–16. https://doi.org/10.1038/s41598-020-58123-2

884 Sanchez, R., Yang, X., Maher, T., & Mackenzie, S. A. (2019). Discrimination of DNA
885   methylation signal from background variation for clinical diagnostics. *International Journal*
886   *of Molecular Sciences*, *20*(21), 5343. https://doi.org/10.3390/ijms20215343

887 Scheufen, T., Krämer, W. E., Iglesias-Prieto, R., & Enríquez, S. (2017). Seasonal variation
888   modulates coral sensibility to heat-stress and explains annual changes in coral productivity.
889   *Scientific Reports*, *7*(1), 4937. https://doi.org/10.1038/s41598-017-04927-8

890 Simpson, C., Herrera-Cubilla, A., & Jackson, J. B. C. (2020). How colonial animals evolve.
891   *Science Advances*, *6*(2), 1–9. https://doi.org/10.1126/sciadv.aaw9530

892 Stadler, J., & Richly, H. (2017). Regulation of DNA repair mechanisms: How the chromatin
893   environment regulates the DNA damage response. In *International Journal of Molecular*
894   *Sciences* (Vol. 18, Issue 8). MDPI AG. https://doi.org/10.3390/ijms18081715

895 Szklarczyk, D., Morris, J. H., Cook, H., Kuhn, M., Wyder, S., Simonovic, M., Santos, A.,
896   Doncheva, N. T., Roth, A., Bork, P., Jensen, L. J., & Von Mering, C. (2017). The STRING
897   database in 2017: Quality-controlled protein-protein association networks, made broadly
898   accessible. *Nucleic Acids Research*, *45*(D1), D362–D368.
899   https://doi.org/10.1093/nar/gkw937

900 Taubner, I., Hu, M. Y., Eisenhauer, A., & Bleich, M. (2019). Electrophysiological evidence for
901   light-activated cation transport in calcifying corals. *Proceedings of the Royal Society B:*
902   *Biological Sciences*, *286*(1896). https://doi.org/10.1098/rspb.2018.2444

903 Torda, G., Donelson, J. M., Aranda, M., Barshis, D. J., Bay, L., Berumen, M. L., Bourne, D. G.,
904   Cantin, N., Foret, S., Matz, M., Miller, D. J., Moya, A., Putnam, H. M., Ravasi, T., van
905   Oppen, M. J. H., Thurber, R. V., Vidal-Dupiol, J., Voolstra, C. R., Watson, S. A., …
906   Munday, P. L. (2017). Rapid adaptive responses to climate change in corals. In *Nature*
907   *Climate Change* (Vol. 7, Issue 9, pp. 627–636). Nature Publishing Group.
908   https://doi.org/10.1038/nclimate3374

909 Trench, R. K. (1993). Microalgal-Invertebrate symbioses : a Review. *Endocytobiosis & Cell*
910   *Research*, *9*, 135–175.

911 Trigg, S. A., Venkataraman, Y. R., Gavery, M. R., Roberts, S. B., Bhattacharya, D., Downey-
912   Wall, A., Eirin-Lopez, J. M., Johnson, K. M., Lotterhos, K. E., Puritz, J. B., & Putnam, H.
913   M. (2022). Invertebrate methylomes provide insight into mechanisms of environmental
914   tolerance and reveal methodological biases. *Molecular Ecology Resources*, *22*(4), 1247–
915   1261. https://doi.org/10.1111/1755-0998.13542

916 Vasquez Kuntz, K. L., Kitchen, S. A., Conn, T. L., Vohsen, S. A., Chan, A. N., Vermeij, M. J.
917   A., Page, C., Marhaver, K. L., & Baums, I. B. (2022). Inheritance of somatic mutations by
918   animal offspring. *Science Advances*, *8*(35), 31. https://doi.org/10.1126/sciadv.abn0707
919 Vásquez-Elizondo, R. M., Legaria-Moreno, L., Pérez-Castro, M. Á., Krämer, W. E., Scheufen,
920   T., Iglesias-Prieto, R., & Enríquez, S. (2017). Absorptance determinations on multicellular
921   tissues. *Photosynthesis Research*, *132*(3), 311–324. https://doi.org/10.1007/s11120-017-
922   0395-6
923 Verhoeven, K. J. F., Jansen, J. J., van Dijk, P. J., & Biere, A. (2010). Stress-induced DNA
924   methylation changes and their heritability in asexual dandelions. *New Phytologist*, *185*(4),
925   1108–1118. https://doi.org/10.1111/j.1469-8137.2009.03121.x
926 Verhoeven, K. J. F., VonHoldt, B. M., & Sork, V. L. (2016). Epigenetics in ecology and
927   evolution: What we know and what we need to know. *Molecular Ecology*, *25*(8), 1631–
928   1638. https://doi.org/10.1111/mec.13617
929 Yang, X., Han, H., DeCarvalho, D. D., Lay, F. D., Jones, P. A., & Liang, G. (2014). Gene body
930   methylation can alter gene expression and is a therapeutic target in cancer. *Cancer Cell*,
931   *26*(4), 577–590. https://doi.org/10.1016/j.ccr.2014.07.028
932 Yang, X., & Mackenzie, S. A. (2020). Approaches to Whole-Genome Methylome Analysis in
933   Plants. In *Methods in Molecular Biology* (Vol. 2093, pp. 15–31). Humana Press Inc.
934   https://doi.org/10.1007/978-1-0716-0179-2_2
935 Yang, X., Sanchez, R., Kundariya, H., Maher, T., Dopp, I., Schwegel, R., Virdi, K., Axtell, M. J.,
936   & Mackenzie, S. A. (2020). Segregation of an MSH1 RNAi transgene produces heritable
937   non-genetic memory in association with methylome reprogramming. *Nature
938   Communications*, *11*(1). https://doi.org/10.1038/s41467-020-16036-8
939 Zhang, J., Zhang, Y. Z., Jiang, J., & Duan, C. G. (2020). The Crosstalk Between Epigenetic
940   Mechanisms and Alternative RNA Processing Regulation. In *Frontiers in Genetics* (Vol.
941   11). Frontiers Media S.A. https://doi.org/10.3389/fgene.2020.00998
942
943

Figures and Tables
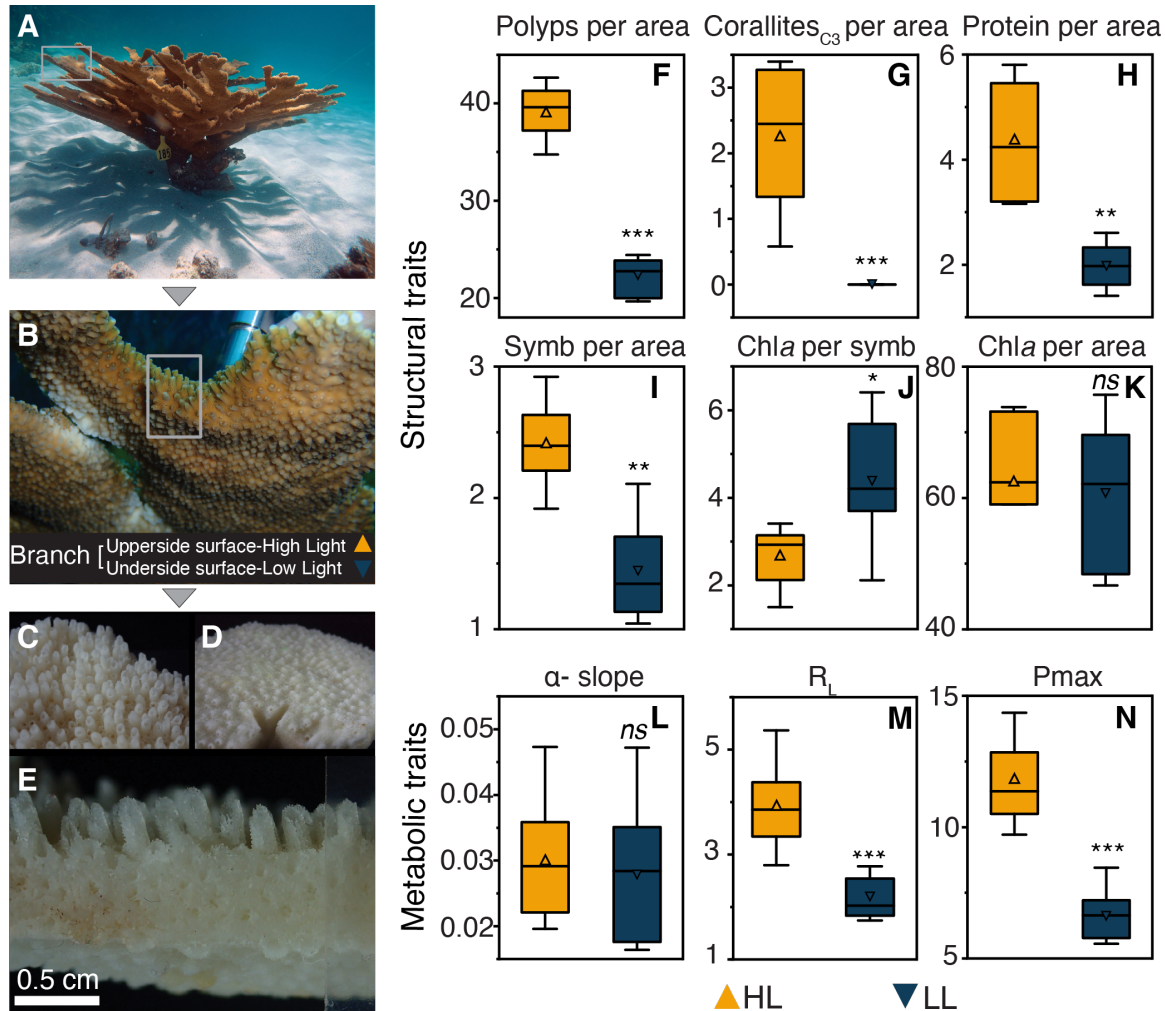
Figure 1. Phenotypic plasticity of *Acropora palmata* in response to light availability. (A) *A. palmata* colonies have a strong intracolonial light gradient. The branching morphology exhibits modules (polyps) exposed to direct sunlight (HL surfaces) and modules growing in the shade (LL surfaces). (**B**) Morphological skeletal features of the branch cross-section showing the transition from upperside to underside of the branch. (**C**) HL surfaces and (**D**) LL surfaces show distinct skeletal morphology, (**E**) with corallites significantly taller in the surface exposed to HL. (**F-N**) Phenotypic traits of HL (n= 21) and LL surfaces (n=21) from 3 genets. Center lines show the median and center squares the mean; box limits indicate the 25th and 75th percentiles; whiskers extend 1 time the interquartile range. For all panels, ***P <0.001; **P <0.01; *P<0.05; *ns*P >0.05, two-tailed, unpaired Student's *t* test. (**F**) Polyp density (# polyps cm^{-2}), (**G**) Density of corallites larger than 3 mm in height (# polyps cm^{-2}), (**H**) soluble host protein (mg protein cm^{-2}), (**I**) symbiont density (# sym cm^{-2}), (**J**) Chl*a* per symbiont cell (Ci, pg Chl*a* sym^{-1}), (**K**) Chl*a* density (mg Chl*a* m^{-2}), (**L**) photosynthetic efficiency (µmol O$_2$ µmol quanta), (**M**) respiration rate (µmol O$_2$ m^{-2} s^{-1}), (**N**) maximum photosynthetic rate (µmol O$_2$ m^{-2} s^{-1}).
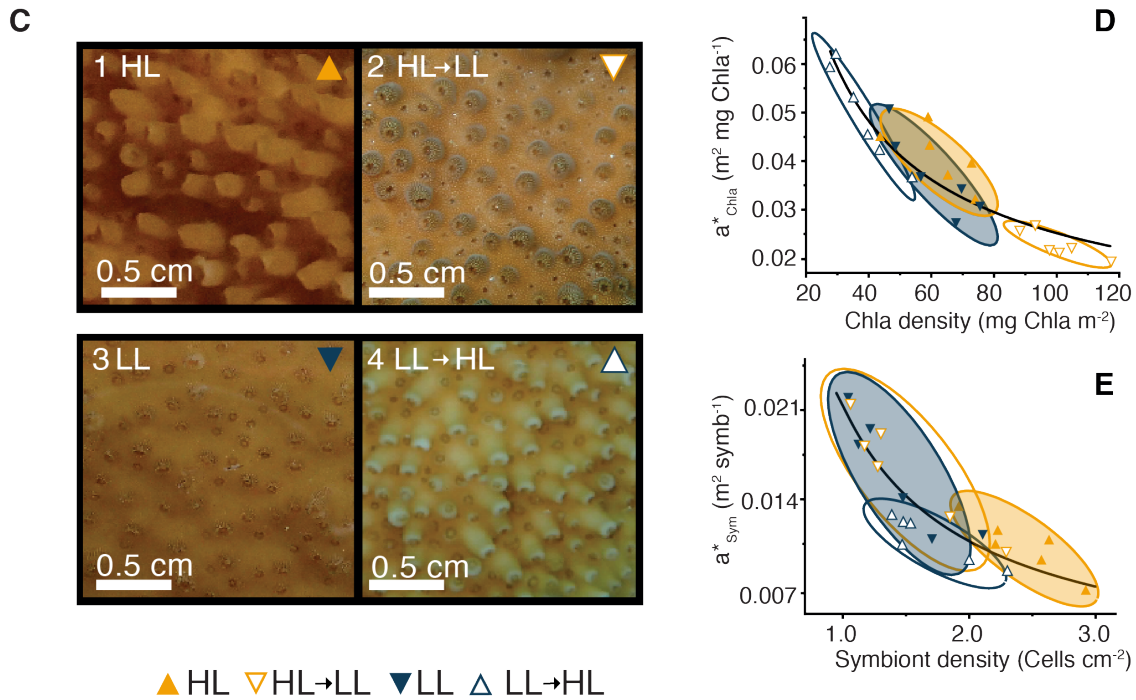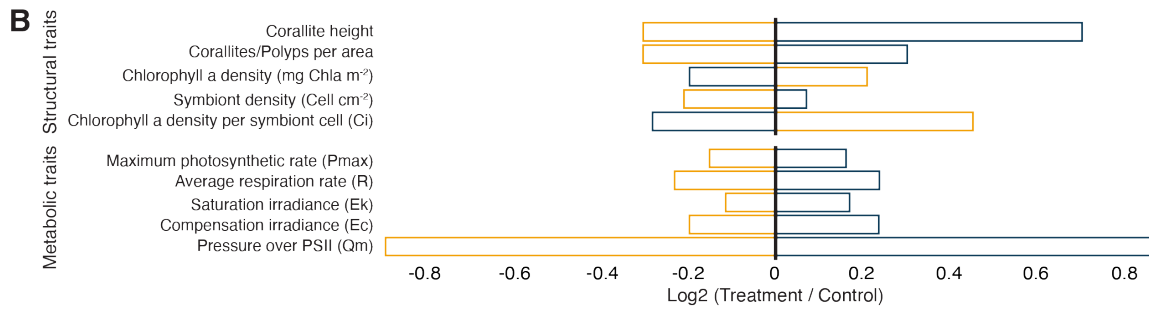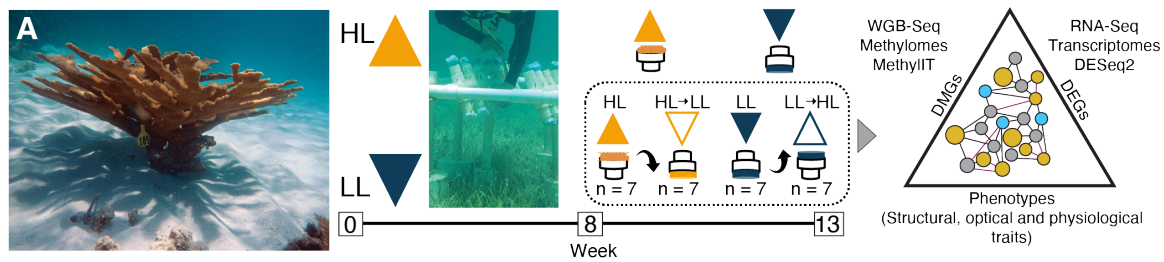
Figure 2. Induced phenotypic plasticity with reciprocal transplants. (**A**) Schematic representation of the experimental design. Control fragments from HL (n=7 per genet) and LL (n=7 per genet) remained unchanged, while treatment fragments (HL→LL, n=7 per genet; LL→HL, n=7 per genet) were manipulated in a reciprocal transplant that altered their light exposure by ~80%. After 13 weeks, light phenotypes were described, and tissue was collected for genomic and epigenomic analyses. (**B**) Fold change of main phenotypic traits showing the acclimatory mechanism to the destination light condition. (**C**) Visual inspection of one genet after 5+ weeks showing the change in corallite height and density. (**D-E**) Changes in optical traits based on specific absorption coefficients, a^*_{Chla} which describes the holobiont's efficiency to absorb light and a^*_{sym} , which describes *in hospite* light absorption efficiency of the algal symbionts.

973
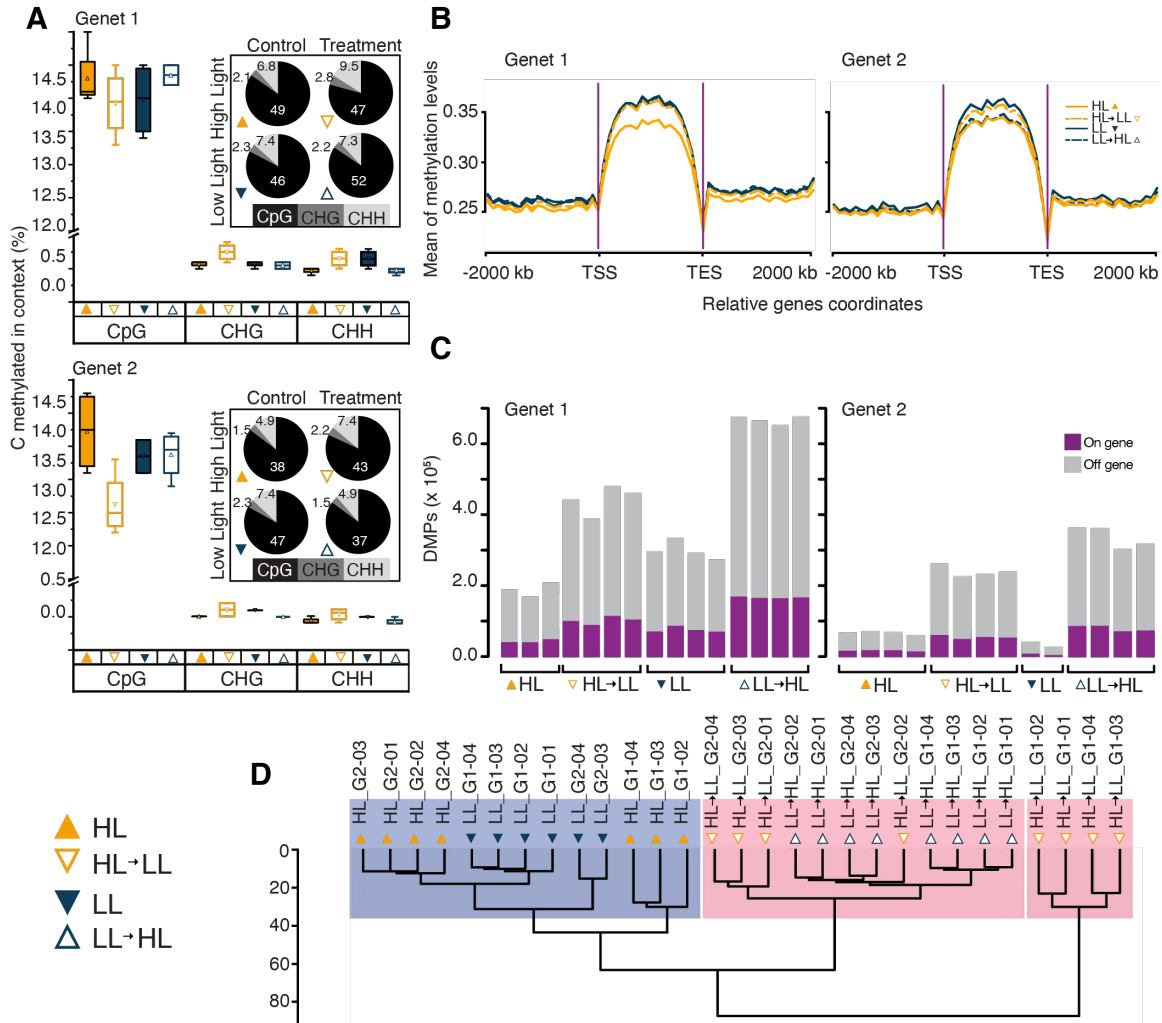
974
Figure 3. DNA Methylation context and light-mediated methylome repatterning. (**A**) Proportion of methylated cytosines (n = 8 per group condition) where highest in the CpG context and insignificant in CHG, and CHH contexts. Pie charts show the number of Cytosines (x 10^6) in each context. (**B**) Mean methylation levels of all cytosines were highest at genic regions; 2kb upstream of Transcription Start Site (TSS), and 2kb downstream of Transcription End Site (TES) are shown. Methylation levels were computed, divided to 60 bins, and plotted by genet and group condition. (**C**) Number of DMPs per group conditions identified by Methyl-IT, with centroid of control groups used as reference. DMPs were always higher in treatments than control samples. Two *A. palmata* genets are shown for comparison. (**D**) Hierarchical clustering of DMPs in genic regions classified by Hellinger Divergence. Classification of samples separated control (purple) and treatment (red) samples regardless of genet or destination light treatment.

985
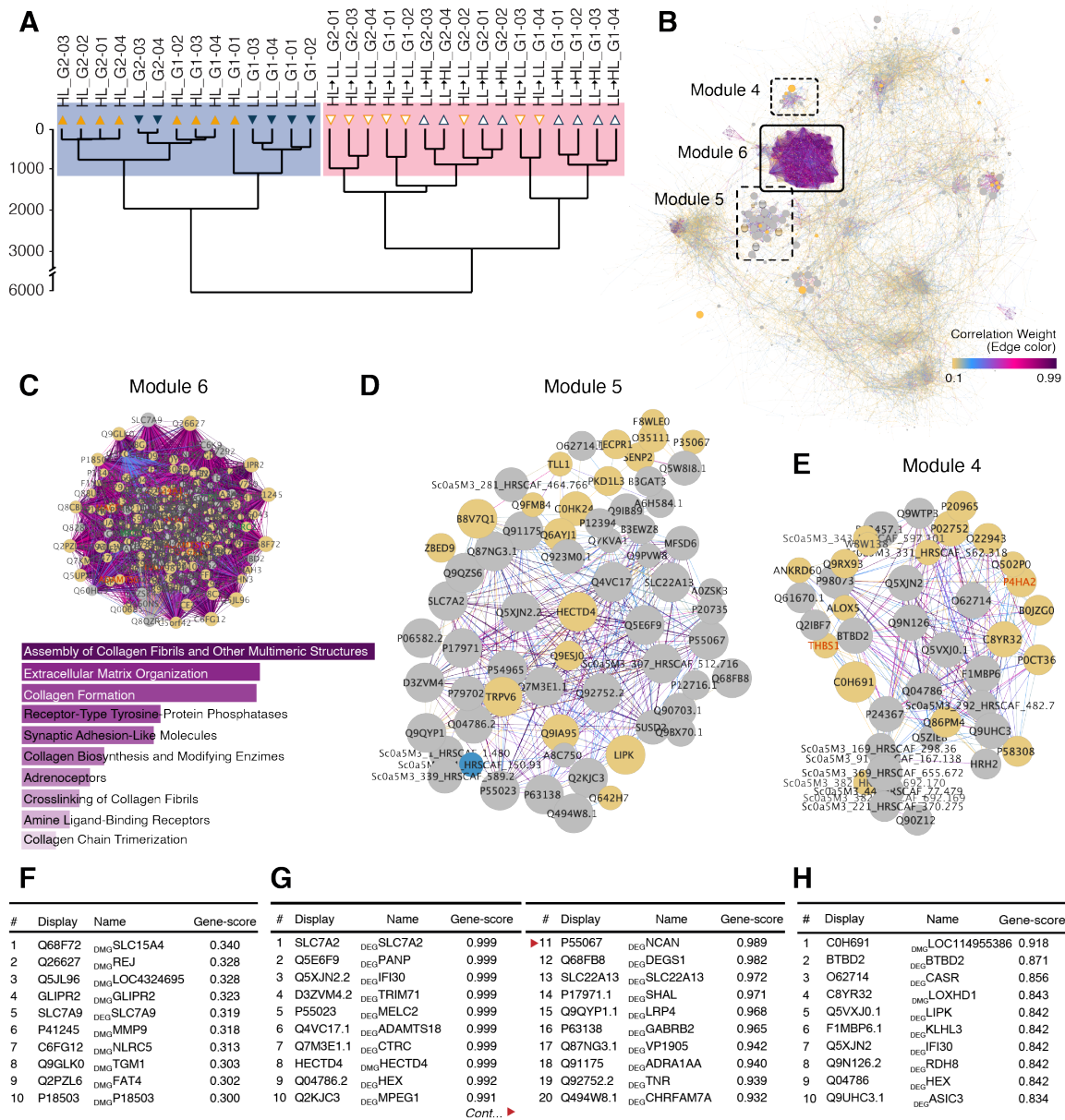
Figure 4. Methylomes-transcriptomes-derived agnostic network, analysis with WGCNA. The data was prepared by combining DMG and DEG datasets to one large dataset. To estimate the initial number of possible groups we performed a (**A**) hierarchical clustering (Ward's agglomeration algorithm), which showed a classification of samples separating controls (purple) and treatments (red) groups regardless of genet or destination light treatment. PCA (PC1 and PC2 carried 92% of the total sample variance) and a linear discriminant analysis (**Fig. S7**) were further performed to assign gene discriminatory power from PC-scores (gene-score) and build the pairwise correlation matrix (Kendal's tau correlation). The network was constructed in WGCNA 1.71, with module visualization and statistical analysis in Cytoscape 3.8.2. (**B**) Whole network of gene-gene interactions. (**C**) Type I subnetwork showing genes with strongest gene-gene interactions (edges with strongest weights from correlation but low gene-score), denotating genes that have similar contribution to the change in phenotype (n = 199 genes). (**D, E**) Type II subnetworks of hub genes showing strong interactions and loadings (highest gene-scores), denotes hub genes with strongest contribution to the change in phenotype (discriminatory power of treatments from controls). (**F-H**) Top 10-20 genes based on gene-score in each subnetwork. The colored line between genes represents weight

38

1001   values from correlation matrix, low weight values (yellow) to high weight values (purple), node color indicates
1002   if DMG (yellow), both DMG-DEG (blue), DEG (grey).
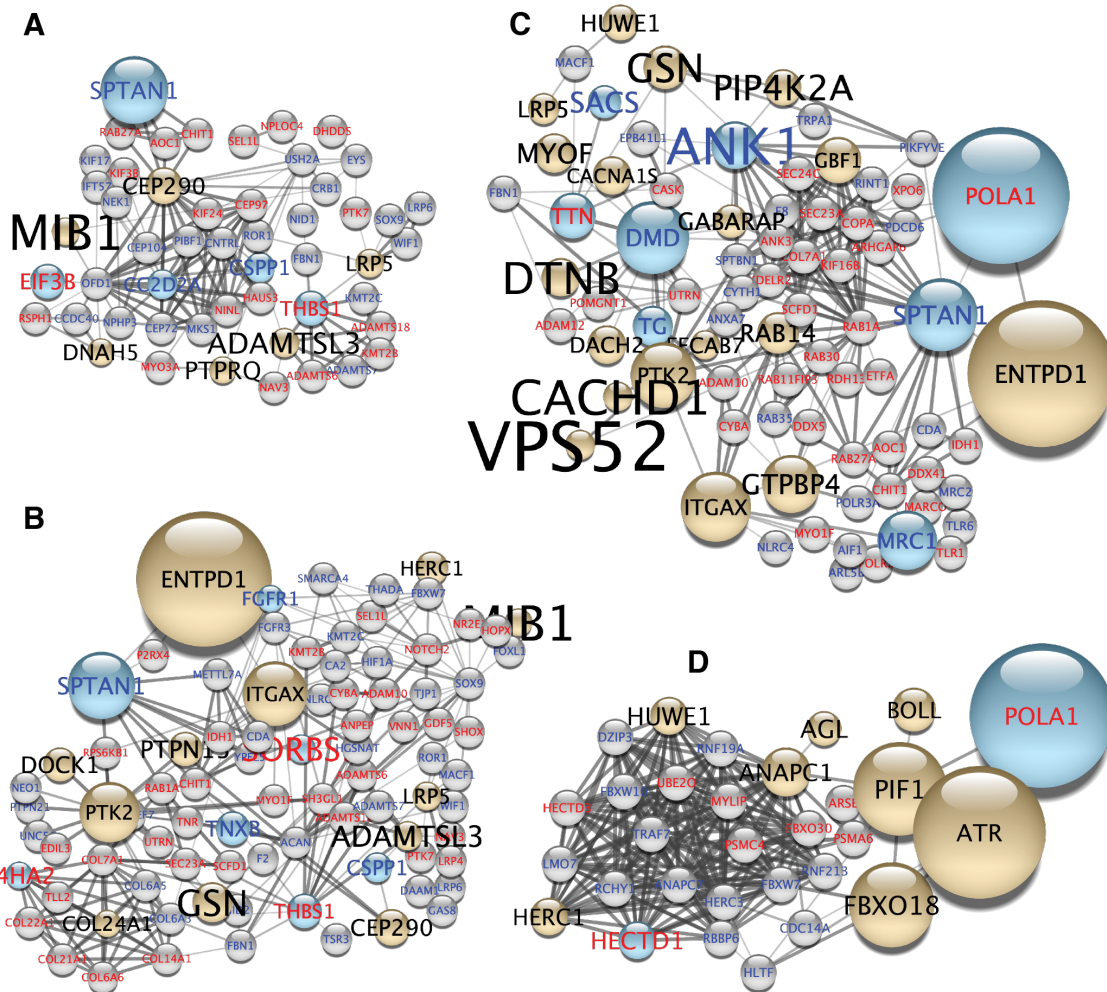
1004
1005 **Figure 5. Predicted network-associated responses from DMGs and DEGs.** Main subnetworks of hub
1006 genes retrieved from integration of DMGs and DEGs. (**A**) photoreception-phototransduction (network from
1007 StringApp without attributes: https://version11.string-db.org/cgi/network.pl?networkId=sqcU0gyKux2Y). (**B**)
1008 ECM-proteins, cell-cell adhesion and EGF-domains associated with soft tissue growth and calcification
1009 (network from StringApp without attributes: https://version11.string-
1010 db.org/cgi/network.pl?networkId=8RQKxPbg9zzZ). (**C**) Vesicle/vacuole mediated transport, Ca^{2+}
1011 metabolism and cytoskeletal protein binding associated with symbiont trafficking (network from StringApp
1012 without attributes: https://version11.string-db.org/cgi/network.pl?networkId =Cefq2PjoZN5R). (**D**) Innate
1013 immune response associated to interpartner recognition (network from StringApp without attributes:
1014 https://version11.string-db.org/cgi/network.pl?networkId= pZerNp9HZxM0). Larger nodes indicate key
1015 regulators or a critical target of a regulatory pathway. The line between genes represents interactions. Node
1016 color indicates if DMG (yellow), both DMG-DEG (blue), DEG (grey). Font size represents methylation (signal
1017 density variation from Methyl-IT) and font color up (red) - down (blue) regulation. Genet 1 LL to HL are
1018 shown for interpretation.
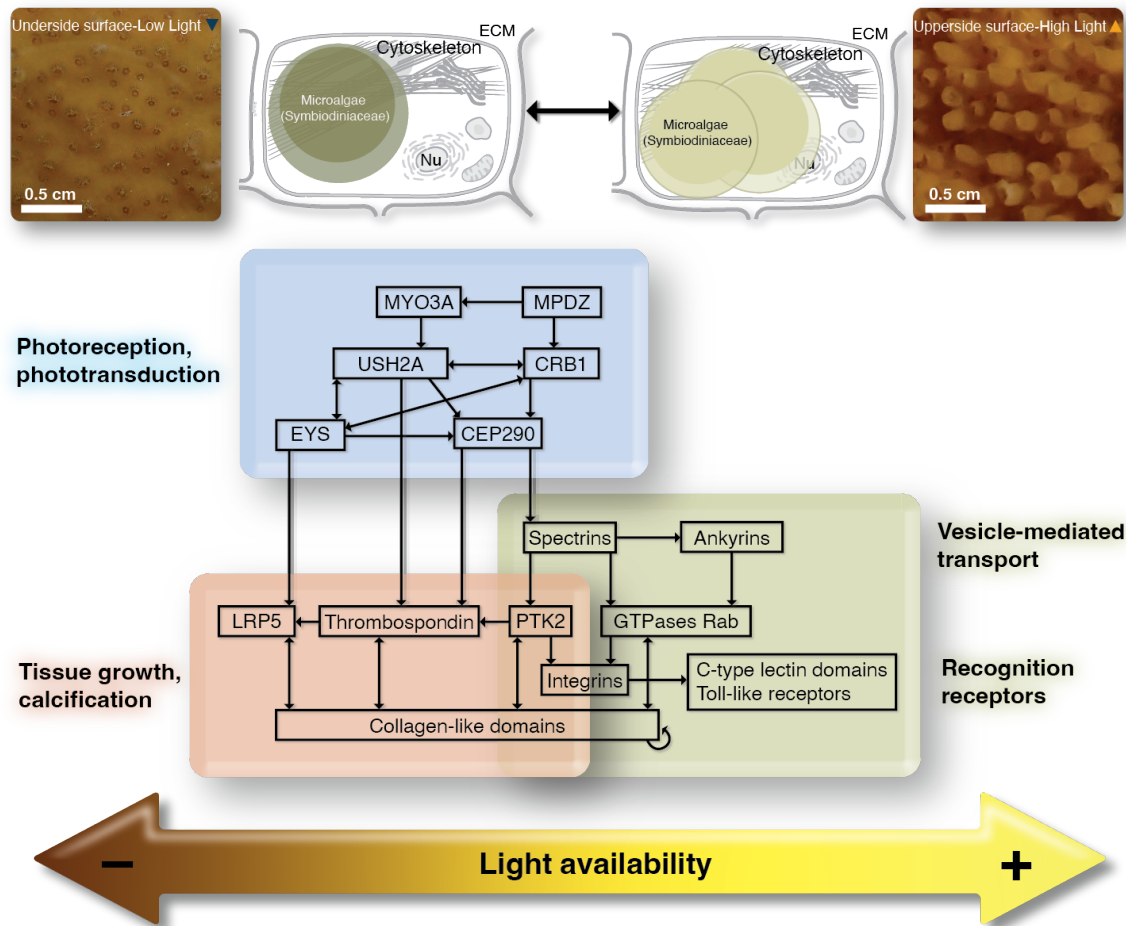
Figure 6. Predicted model for light-mediated phenotypic plasticity of structural traits in the branching coral *Acropora palmata* based on key regulators from DMGs-DEGs integrated networks. A significant change in the light environment activates photoreception mechanisms to detect cues and transduce information within cells (symbionts, cytoskeleton, extra cellular matrix-ECM, and nucleus-Nu are labeled). This activates signaling pathways to control growth, both soft tissue and skeletal growth; and in parallel, to initiate cellular transport related to symbiont recognition and changes in symbiont population densities (network from StringApp without attributes: https://version11.string-db.org/cgi/network.pl?networkId=uh6Y1lbNXqJR).

1028 **Table 1. Table of terms, definitions, and units for the structural, optical, and photosynthetic**
1029 **parameters used to describe phenotypes.**

Traits	Parameters	Units
Structural	Corallite density at height class:	
	$\quad$ C_1: 0 - 1.5 mm height,	# C_{H1}-corallites cm^{-2}
	$\quad$ C_2: >1.5 - 3 mm height,	# C_{H2}-corallites cm^{-2}
	$\quad$ C_3: >3 mm height	# C_{H3}-corallites cm^{-2}
	Total polyp density	# corallites cm^{-2}
	Soluble host protein per projected area	mg protein cm^{-2}
	Chl$a$ density per projected area	mg Chl$a$ m^{-2}
	Algal density per projected area	#sym cm^{-2}
	Chl$a$ per algal cell (Ci)	pg Chl$a$ sym^{-1}
Optical	Host mass-specific absorption efficiency (a^*_M)	cm^2 mg protein^{-1}
	Light absorption efficiency of symbionts *in hospite* (a^*_{Sym})	m^2 sym^{-1}
	Light absorption efficiency of the holobiont (a^*_{Chla})	m^2 mg Chla^{-1}
	Estimated Absorbance (De 675 nm)	Dimensionless
Physiological	Photosynthetic efficiency (α)	µmol O_2 µmol quanta
	Minimum Quantum Requirement (Φ^{-1}_{O2})	mol photons mol^{-1}_{O2}
	Maximum gross photosynthetic rate per area (Pmax)	µmol O_2 m^{-2} s^{-1}
	Saturation irradiance (E_k)	µmol quanta m^{-2} s^{-1}
	Compensation irradiance (E_c)	µmol quanta m^{-2} s^{-1}
	Post-illumination respiration rate (R_L)	µmol O_2 m^{-2} s^{-1}
	Pressure over Photosystem II (Q_m)	Dimensionless

1030
1031
1032